












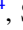




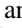




# Photometric Observations of the Binary Near-Earth Asteroid (65803) Didymos in 2015–2021 Prior to DART Impact

P. Pravec<sup>1</sup> , C. A. Thomas<sup>2</sup> , A. S. Rivkin<sup>3</sup> , P. Scheirich<sup>1</sup> , N. Moskovitz<sup>4</sup> , M. M. Knight<sup>5,6</sup> , C. Snodgrass<sup>7</sup> , J. de León<sup>8</sup> , J. Licandro<sup>8</sup> , M. Popescu<sup>9,8</sup>, A. Thirouin<sup>4</sup> , D. Föhring<sup>10,11</sup>, C. O. Chandler<sup>2</sup> , W. J. Oldroyd<sup>2</sup> , C. A. Trujillo<sup>2</sup> , E. S. Howell<sup>12</sup>, S. F. Green<sup>13</sup>, J. Thomas-Osip<sup>14</sup>, S. S. Sheppard<sup>15</sup> , T. L. Farnham<sup>6</sup> , E. Mazzotta Epifani<sup>16</sup>, E. Dotto<sup>16</sup>, S. Ieva<sup>16</sup> , M. Dall’Ora<sup>17</sup> , R. Kokotanekova<sup>18,19</sup> , B. Carry<sup>20</sup> , and D. Souami<sup>21,22</sup>

<sup>1</sup> Astronomical Institute, Academy of Sciences of the Czech Republic, Fričova 1, CZ-25165 Ondřejov, Czech Republic; [petr.pravec@asu.cas.cz](mailto:petr.pravec@asu.cas.cz)

<sup>2</sup> Department of Physics and Astronomy, Northern Arizona University, PO Box 6010, Flagstaff, AZ 86011, USA

<sup>3</sup> JHU/APL, 11100 Johns Hopkins Road, Laurel, MD 20723, USA

<sup>4</sup> Lowell Observatory, 1400 West Mars Hill Road, Flagstaff, AZ 86001, USA

<sup>5</sup> Department of Physics, United States Naval Academy, 572C Holloway Road, Annapolis, MD 21402, USA

<sup>6</sup> Department of Astronomy, University of Maryland, College Park, MD 20742, USA

<sup>7</sup> Institute for Astronomy, University of Edinburgh, Royal Observatory, Edinburgh EH9 3HJ, UK

<sup>8</sup> Instituto de Astrofísica de Canarias (IAC), C/Vía Láctea s/n, E-38205 La Laguna, Spain

<sup>9</sup> Astronomical Institute of the Romanian Academy, 5 Cuștău de Argint, 040557 Bucharest, Romania

<sup>10</sup> Institute for Astronomy, University of Hawai‘i, 2680 Woodlawn Drive, Honolulu, HI 96822, USA

<sup>11</sup> ESA NEO Coordination Centre, Largo Galileo Galilei, 1, I-00044 Frascati (RM), Italy

<sup>12</sup> Lunar and Planetary Laboratory, University of Arizona, Tucson, AZ 85721, USA

<sup>13</sup> School of Physical Sciences, The Open University, Milton Keynes, MK7 6AA, UK

<sup>14</sup> Gemini Observatory/NSF’s NOIRLab, Casilla 603, La Serena, Chile

<sup>15</sup> Carnegie Institution for Science, Earth and Planets Laboratory, 5241 Broad Branch Road NW, Washington, DC 20015, USA

<sup>16</sup> INAF–Osservatorio Astronomico di Roma, Via Frascati 33, I-00040 Monte Porzio Catone (RM), Italy

<sup>17</sup> INAF–Osservatorio Astronomico di Capodimonte, Salita Moiariello 16, I-80131 Napoli, Italy

<sup>18</sup> European Southern Observatory, Karl-Schwarzschild-Str 2, D-85748 Garching, Germany

<sup>19</sup> Institute of Astronomy, Bulgarian Academy of Sciences, Sofia, Bulgaria

<sup>20</sup> Université Côte d’Azur, Observatoire de la Côte d’Azur, CNRS, Laboratoire Lagrange, France

<sup>21</sup> LESIA, Observatoire de Paris, Université PSL, Sorbonne Université, Université de Paris, CNRS, F-92190 Meudon, France

<sup>22</sup> naXys, University of Namur, 8 Rempart de la Vierge, Namur, B-5000, Belgium

Received 2021 November 19; revised 2022 June 20; accepted 2022 June 21; published 2022 July 27

## Abstract

We performed photometric observations of the binary near-Earth asteroid (65803) Didymos in support of the Double Asteroid Redirection Test (DART) mission that will test the Kinetic Impactor technology for diverting dangerous asteroids. It will hit the Didymos secondary, called Dimorphos, on 2022 September 26. We observed Didymos with 11 telescopes with diameters from 3.5 to 10.4 m during four apparitions in 2015–2021, obtaining data with rms residuals from 0.006 to 0.030 mag. We analyzed the light-curve data and decomposed them into the primary rotational and secondary orbital light curves. We detected 37 mutual eclipse/occultation events between the binary system components. The data presented here, in combination with 18 mutual events detected in 2003, provide the basis for modeling the Dimorphos orbit around the Didymos primary. The orbit modeling is discussed in detail by Scheirich & Pravec and Naidu et al. The primary light curves were complex, showing multiple extrema on some epochs. They suggest a presence of complex topography on the primary’s surface that is apparent in specific viewing/illumination geometries; the primary shape model by Naidu et al. (Icarus 348, 113777, 2020) needs to be refined. The secondary rotational light-curve data were limited and did not provide a clear solution for the rotation period and equatorial elongation of Dimorphos. We define the requirements for observations of the secondary light curve to provide the needed information on Dimorphos’s rotation and elongation when Didymos is bright in 2022 July–September before the DART impact.

*Unified Astronomy Thesaurus concepts:* Asteroid satellites (2207); CCD photometry (208); Near-Earth objects (1092)

## 1. Introduction

The near-Earth asteroid (65803) Didymos, originally designated 1996 GT, was discovered by the Spacewatch asteroid survey from Kitt Peak Observatory in Arizona on 1996 April 11. Seven years later, it was thoroughly studied with photometric and radar observations around and after its close approach to Earth in 2003 November, which led to the

discovery of its satellite with photometric observations taken from Ondřejov Observatory, Carbuncle Hill Observatory, and Steward Observatory during 2003 November 20–24 and radar observations from Arecibo on 2003 November 23 and 24 (Pravec et al. 2003). The photometric observations were analyzed and modeled in Pravec et al. (2006) and Scheirich & Pravec (2009), where they published initial estimates of several parameters of the binary asteroid system, including first estimates of the secondary (satellite) orbit around the primary body of the binary system. The radar observations were published and modeled together with the photometric data by Naidu et al. (2020), who obtained a shape model of the primary



Original content from this work may be used under the terms of the [Creative Commons Attribution 4.0 licence](https://creativecommons.org/licenses/by/4.0/). Any further distribution of this work must maintain attribution to the author(s) and the title of the work, journal citation and DOI.

and determined or constrained several parameters of the binary asteroid system. The current best estimates for the parameters of the primary and secondary and their mutual orbit are given in Scheirich & Pravec (2022), and we give the nominal values for some of them in the following. The volume-equivalent diameters of the primary and secondary are 0.78 and 0.17 km, respectively. The geometric albedo in the  $V$  band is 0.15. The mutual orbit is retrograde with the J2000 ecliptic coordinates of the pole  $(L_p, B_p) = (320^\circ.6, -78^\circ.6)$ , with a semimajor axis of 1.19 km and an orbital period of 11.9216 hr. Spectral observations taken in 2003 originally classified Didymos as an Xk type (Binzel et al. 2004), but later analyses led to a consensus on a silicate composition for the binary system (de León et al. 2006, 2010; Dunn et al. 2013). New spectral observations obtained in 2021 have confirmed its silicate nature, with hints of possible small spectral variability with the primary’s rotation (Ieva et al. 2022).

The secondary of the Didymos binary system, recently named Dimorphos, has been selected as a target of the Double Asteroid Redirection Test (DART). DART is NASA’s first planetary defense test mission, demonstrating the kinetic impactor mitigation technique. It launched from Vandenberg Space Force Base in 2021 November and will arrive at the Didymos system and impact into Dimorphos on 2022 September 26. The main benefit of using a binary asteroid system for a kinetic impactor mission is that it allows the results of the test to be measured from Earth via photometric measurements, assuming that the binary system exhibits mutual events seen from Earth.<sup>23</sup> Mutual events in the Didymos system can be seen from Earth, making it a suitable target. Rivkin et al. (2021) discussed the factors that led to the recognition that Didymos was the best candidate for a kinetic impactor test and its selection as the DART target system. Several years after the DART impact, the Didymos system will be visited by ESA’s Hera mission, which will provide a thorough description of the postimpact state of the binary system (Michel et al. 2022).

An important part of the preparation of the DART mission has been an observational effort to determine the parameters of the binary asteroid system. The most significant mission-critical task has been the effort to precisely determine the orbit of the secondary around the primary. For that, we have used the method of photometric observations of mutual events between binary asteroid system components (Pravec et al. 2006), which we have applied to photometric observations taken with several large- or medium-sized ground-based telescopes from 2015 to 2021. In this paper, we present the results of this major observational campaign. The photometric observations are presented in Section 2. In Section 3, we present decompositions of the photometric data into the primary rotational and secondary orbital light-curve components for individual epochs covered by the observations. The data for the mutual events between the two bodies of the binary asteroid obtained from the derived secondary orbital light-curve components have been used for modeling the secondary orbit by Naidu et al. (2022) and Scheirich & Pravec (2022). In Section 4, we analyze the

constraints provided by the secondary rotational light-curve data (outside mutual events) on the equatorial elongation of the secondary.

## 2. Observations

The photometric observations taken in the Dimorphos discovery apparition in 2003 were published in Pravec et al. (2006). We summarize them in the first part of Table 1. The observations were taken with small telescopes with diameters from 0.35 to 1.5 m. Thanks to the high brightness of Didymos in the favorable observing conditions shortly after its close approach to Earth in November 2003, with visual magnitude  $V$  in the range from 12.9 to 14.9, they were of high quality; the median rms residual of Fourier series fits to them is 0.008 ma (see Section 3). As will be seen below, the 2003 data are the highest-quality data subset of all five observed apparitions of Didymos and the second most abundant (after the last apparition of 2020–2021) in number of observed mutual events. In addition, these data were taken with Didymos at heliocentric true anomaly values from  $27^\circ$  to  $53^\circ$ , which were not covered in the 2015–2021 apparitions. Thus, the 2003 data provided a great baseline for accurate determination of Dimorphos’s orbit.

Shortly after the satellite of the Didymos binary system was selected as the target of the DART mission, we realized the need to make many more photometric observations in order to determine its mutual orbit with high accuracy. As Didymos’s heliocentric orbit period is 2.109 yr, its oppositions with the Sun occurred at nearly 2 yr intervals during 2015–2021. (The heliocentric synodic period of Didymos is  $(1 - 2.109^{-1})^{-1} = 1.902$  yr.) Unlike in the 2003 apparition, when Didymos was near perihelion and close to Earth and thus very bright, it was much more distant during the years 2015–2021. The four oppositions in 2015, 2017, 2019, and 2021 occurred at heliocentric true anomalies  $>119^\circ$ ; i.e., Didymos was far from the perihelion of its eccentric orbit ( $e = 0.384$ ). It was therefore much fainter during the four follow-up apparitions than in 2003, with  $V$  in the range from 19.0 to 21.5 on individual observing nights. We therefore required medium- to large-sized telescopes to obtain data of acceptable quality for the task of detecting mutual events in the binary system and modeling Dimorphos’s orbit around the primary.

The observations are summarized in Table 1. Each row in the table represents one nightly run with one telescope, identified with the mid-UTC date of the session rounded to the nearest tenth of a day in the first column. Subsequent columns give the telescope or station name, the telescope’s diameter, the number of photometric data points obtained, the duration of the session, and a reference to where more information on the observations is available.

As shown in Table 1, the first photometric observations since 2003 were taken with the 4.3 m Discovery Channel Telescope (DCT; which has since been renamed the Lowell Discovery Telescope, LDT) in Arizona on 2 nights in 2015 April. They gave only a limited quantity of medium-quality data with an rms residual of 0.024 mag (see the analysis in Section 3 and Table 2), and we realized that we would need to take many more data and use larger telescopes, or medium-sized telescopes in excellent observing conditions, to obtain the required high-quality data for Didymos in the following apparitions. In 2017, we used several telescopes with sizes from 3.5 to 10.4 m and obtained more abundant data, although their quality was largely similar to those of the 2015 observations. We succeeded in obtaining

<sup>23</sup> DART will also perform a limited characterization of the Didymos system around the impact time. It will carry the ASI Light Italian Cubesat for Imaging of Asteroid (LICIACube; Dotto et al. 2021) as a piggyback. The LICIACube will perform an autonomous flyby of the Didymos system probing the DART impact, and it will study the structure and evolution of the ejecta plume produced by the impact, which is expected to bring fundamental information for the determination of the momentum transfer induced by DART.

**Table 1**  
Photometric Observations of (65803) Didymos

Session Mid-UT	Station/Telescope	Diam. (m)	Points	Dur. (hr)	References
2003-11-20.9	Ondřejov	0.65	296	4.1	P06
2003-11-22.0	Ondřejov	0.65	315	6.0	P06
2003-11-22.2	Carbuncle Hill	0.35	102	5.6	P06
2003-11-23.2	Carbuncle Hill	0.35	89	4.8	P06
2003-11-24.2	Mt. Lemmon	1.5	252	6.2	P06
2003-11-24.3	Carbuncle Hill	0.35	57	3.4	P06
2003-11-26.2	Carbuncle Hill	0.35	97	5.8	P06
2003-11-27.9	Ondřejov	0.65	146	4.2	P06
2003-11-30.0	Ondřejov	0.65	283	8.2	P06
2003-12-2.2	Carbuncle Hill	0.35	79	5.0	P06
2003-12-3.3	Palmer Divide	0.50	106	7.8	P06
2003-12-4.1	Carbuncle Hill	0.35	67	5.6	P06
2003-12-16.9	Ondřejov	0.65	15	0.8	P06
2003-12-17.3	Palmer Divide	0.50	146	9.2	P06
2003-12-18.9	Ondřejov	0.65	95	10.0	P06
2003-12-19.3	Palmer Divide	0.50	75	7.7	P06
2003-12-20.3	Palmer Divide	0.50	127	7.1	P06
2015-4-13.3	DCT	4.3	75	5.7	Section 2.1
2015-4-14.4	DCT	4.3	45	1.7	Section 2.1
2017-2-23.3	VLT	8.2	17	0.7	Section 2.2
2017-2-24.4	VLT	8.2	15	0.6	Section 2.2
2017-2-25.1	GTC	10.4	75	5.5	Section 2.3
2017-2-25.4	VLT	8.2	17	0.7	Section 2.2
2017-2-25.5	MMT	6.5	137	4.2	Section 2.4
2017-2-27.3	VLT	8.2	31	1.5	Section 2.2
2017-3-1.3	VLT	8.2	12	0.6	Section 2.2
2017-3-31.1	WHT	4.2	100	8.9	Section 2.5
2017-4-1.3	VLT	8.2	27	1.6	Section 2.2
2017-4-2.3	VLT	8.2	17	0.7	Section 2.2
2017-4-18.2	DCT	4.3	66	5.2	Section 2.1
2017-4-27.1	NTT	3.5	108	6.9	Section 2.6
2017-5-4.3	Gemini N	8.1	59	3.8	Section 2.7
2019-1-31.4	DCT	4.3	98	5.6	Section 2.1
2019-2-2.2	Magellan	6.5	21	1.3	Section 2.8
2019-3-9.1	GTC	10.4	166	6.5	Section 2.3
2019-3-10.2	GTC	10.4	65	3.2	Section 2.3
2019-3-11.1	GTC	10.4	143	6.6	Section 2.3
2020-12-12.6	Gemini N	8.1	89	4.1	Section 2.7
2020-12-17.4	LDT	4.3	95	5.3	Section 2.1
2020-12-20.5	LDT	4.3	31	2.2	Section 2.1
2020-12-23.4	LDT	4.3	118	5.8	Section 2.1
2021-1-8.5	LDT	4.3	93	4.8	Section 2.1
2021-1-9.4	LDT	4.3	118	6.0	Section 2.1
2021-1-10.4	LDT	4.3	78	4.8	Section 2.1
2021-1-12.6	Gemini N	8.1	107	4.5	Section 2.7
2021-1-14.4	LDT	4.3	107	5.9	Section 2.1
2021-1-14.6	Keck	10.0	69	4.4	Section 2.9
2021-1-17.5	Gemini N	8.1	142	5.5	Section 2.7
2021-1-18.4	LBT	8.4	150	3.0	Section 2.10
2021-1-20.2	TNG	3.6	296	6.5	Section 2.11
2021-2-17.4	LDT	4.3	121	9.4	Section 2.1
2021-3-6.3	LDT	4.3	149	8.2	Section 2.1

**Note.** P06 is Pravec et al. (2006).

high-quality observations with a median rms residual of 0.010 mag in 2019, although the limited coverage only allowed the detection of five events (see Table 2). Learning from the experience of the 2015–2019 apparitions, in 2020–2021, we obtained much wider data coverage (detecting as many as 23 events) with high quality (the median rms residual was 0.011 mag).

In the following subsections, we describe the observational and reduction techniques we used on the 11 telescopes involved in the observational campaign. We used some common techniques for all or most of the observations, but there were many differences in the observing strategies and reduction techniques used on the individual telescopes or by the

**Table 2**  
Didymos Light-curve Decompositions

Sessions	Points	Events	rms Res. (mag)	$\alpha$ (deg)	$\nu$ (deg)	Plot
2003-11-20.9 to 2003-11-24.3	1111	5	0.008	15.4	27.0	P06
2003-11-26.2 to 2003-12-4.1	778	8	0.008	4.8	34.9	P06
2003-12-16.9 to 2003-12-20.3	458	5	0.012	8.3	52.7	P06
2015-4-13.3 to 2015-4-14.4	120	2	0.024	3.1	168.2	Figure 1
2017-2-23.3 to 2017-3-1.3	304	2	0.017	17.9	146.9	Figure 2
2017-3-31.1 to 2017-4-2.3	144	2	0.025	3.8	155.7	Figure 3
2017-4-18.2 to 2017-5-4.3	233	3	0.030	16.3	161.9	Figure 4
2019-1-31.4 to 2019-2-2.2	119	2	0.011	25.7	126.7	Figure 5
2019-3-9.1 to 2019-3-11.1	374	3	0.010	4.1	138.7	Figure 6
2020-12-12.6 to 2020-12-23.4	333	4	0.011	44.2	87.9	Figure 7
2021-1-8.5 to 2021-1-10.4	289	6	0.010	33.3	100.5	Figure 8
2021-1-12.6 to 2021-1-14.6	283	4	0.008	30.7	102.6	Figure 9
2021-1-17.5 to 2021-1-18.4	292	4	0.006	27.8	104.7	Figure 10
2021-1-20.2	296	2	0.015	26.2	105.8	Figure 11
2021-2-17.4	121	2	0.012	5.2	118.0	Figure 12
2021-3-6.3	149	1	0.011	11.1	124.5	Figure 13

**Note.** P06 is Pravec et al. (2006).

individual observers, and we used several different photometric reduction methods and tools. By that, we effectively checked the mutual consistency of the obtained data, eliminating or reducing the possibility of the presence of systematics in the data that could come from using a single observational technique and reduction pipeline. The common points for all of the observations were as follows. We used CCD detectors, processed the obtained images with standard bias subtraction and flat-field correction routines, and performed aperture photometry on Didymos and reference star images. In the subsections below, we focus primarily on the specifics of the individual observations and data reductions.

### 2.1. Lowell Discovery Telescope

The 4.3 m LDT (known prior to 2020 February as the Discovery Channel Telescope) is located near Happy Jack, Arizona, at an elevation of 2360 m. Images of Didymos were obtained from LDT in every apparition from 2015 to 2021 (Table 1). In all cases, the Large Monolithic Imager (LMI), which is equipped with a  $6k \times 6k$  e2v CCD, was used with a broadband VR filter (covering the wavelengths between about 500 and 700 nm) to maximize the signal-to-noise ratio (S/N). The LMI images a  $12.3$  square field of view that is sampled at an image scale of  $0.12$  pixel $^{-1}$ . All images were obtained in  $3 \times 3$  binning mode, resulting in an effective image scale of  $0.36$  pixel $^{-1}$ . For all nights except for 2021 March 6, the telescope was tracked at sidereal rates, allowing the asteroid to move through a fixed star field. On 2021 March 6, the telescope was tracked at half the nonsidereal rates so that both stars and asteroid were trailed by the same amount (roughly  $1''$ ). Exposure times ranged from 120 to 180 s, chosen to minimize trailing based on the nonsidereal motion of the asteroid and local seeing conditions. Across all apparitions, any images affected by background contamination and/or heavy extinction were removed from further analysis.

The data from 2015 April 14 and 2017 April 18 were analyzed using the standard data reduction described in Thirouin & Sheppard (2018). To summarize our approach, we selected an optimal aperture using the growth curve technique (Stetson 1990) to limit background contamination while including all of the object's flux. Aperture photometry

with the optimal aperture radius was performed with the DAOPHOT routines (Stetson 1987). The data from 2015 April 13 were reduced at Ondřejov Observatory using an analogous optimal aperture photometry method using their *Aphot* software package (Pravec et al. 2006).

The measurement of photometry from the 2019 and 2020–2021 apparitions involved processing images with the PhotometryPipeline (Mommert 2017). This pipeline registers images using Scamp (Bertin 2006) with the Gaia DR2 reference catalog (Gaia Collaboration et al. 2018). Point-source photometry is measured using SExtractor (Bertin & Arnouts 1996). Calibration of the photometry involved converting instrumental to calibrated magnitudes based on field stars with solar-like colors (within 0.2 mag of the Sun's SDSS ( $g - r$ ) and ( $r - i$ ) color indices) in the PanSTARRS DR1 catalog (Flewelling et al. 2020). The photometry was calibrated to the PanSTARRS  $r$  band. In general, about 10 field stars were used to calibrate each frame. An optimized aperture was chosen for each night of observing that minimized the errors associated with the zero-point calibration (i.e., tying to the reference catalog) and the measured instrumental magnitudes. These apertures ranged from 3.26 to 6.63 pixels ( $1.17$ – $2.39$ ) in radius. Though not critical for the differential analysis performed here (Section 3), this resulted in absolute photometric calibration with errors of about 0.02 mag.

In total, the LDT data provided light curves from 13 different nights and sampled part or the entirety of 16 individual mutual events. Light-curve quality from LDT was good on most nights, with the median rms residual relative to the best fits of the primary light curve of 0.011 mag (see Section 3). The apparent  $V$  magnitude of Didymos during these LDT observations ranged from a minimum of about 19.0 in 2021 February to a maximum of about 21.0 in 2017 April.

### 2.2. Very Large Telescope

Observations in 2017 were taken at Unit Telescope 3 (Melipal; UT3) of the European Southern Observatory (ESO) 8 m Very Large Telescope (VLT) using the VIMOS instrument (Le Fèvre et al. 2003). This instrument is primarily a multiobject spectrograph but also has an imaging mode with

an array of four CCDs, each with a  $7 \times 8$  arcmin<sup>2</sup> field of view and  $0''.21$  pixel<sup>-1</sup> scale and standard *UBVRI* filters. Didymos was observed in service mode in a program designed to take advantage of time with relatively poor conditions (for Paranal), when the other instruments on UT3, requiring exceptional seeing, could not be used. Observations were scheduled as independent hour-long blocks, each made up of  $17 \times 120$  s *R*-band exposures, tracking the asteroid at its nonsidereal rate. The telescope was offset to have the asteroid appear approximately in the center of one of the four CCDs. Thirteen blocks were taken between 2017 January 14 and 2017 April 3. The seeing (measured by the Paranal site DIMM) varied between  $0''.36$  and  $3''.2$ , with a median of  $1''.2$ , during the exposures. Useful data were obtained on 7 separate nights, on 2 of which two observing blocks were executed sequentially to have around 1.5 hr of continuous exposures (see Table 1). Aperture photometry was performed using the Image Reduction and Analysis Facility (IRAF), using apertures with a radius of 1.5 times the frame FWHM, and calibrated using field stars from the PanSTARRS PS1 catalog (hereafter PS1; Chambers et al. 2016) after first converting the catalog magnitudes to *UBVRI*. Frames where the asteroid was close to any background source were manually removed from the final light curve.

The 2019 VLT data were taken with FORS on UT1 (Antu), which has a square field of view of  $6'.8$  on each side, across two CCDs, and a  $(2 \times 2)$  binned pixel scale of  $0''.25$  pixel<sup>-1</sup> (Appenzeller et al. 1998). These observations were performed in visitor mode over the nights of 2019 April 5 and 6, with excellent conditions. A total of 511 exposures were taken over the 2 nights, the majority with a 50 s exposure time in the FORS *R\_SPECIAL* filter, which is close to the standard Bessell *R* in wavelength range but with higher peak transmission and sharper cutoffs, particularly at the red end. Basic data reduction was performed using PyRAF tasks, and the photometry was calibrated via field stars appearing in the PS1 catalog, following the techniques described by Kokotanekova et al. (2017). Unfortunately, the presence of reflections from a nearby bright star influenced the photometry and prevented us from achieving the necessary accuracy to separate the primary light curve and mutual events, so this data set is not included in the rest of the analysis.

### 2.3. Gran Telescopio Canarias

Observations with the Gran Telescopio Canarias (GTC) were done in 2017 February and 2019 March when the asteroid had apparent visual magnitude  $V = 21.0$  and  $19.9$ , respectively. The GTC is located at the Roque de Los Muchachos Observatory in La Palma, Canary Islands (Spain), and managed by the Instituto de Astrofísica de Canarias. Images of Didymos were acquired using the Optical System for Imaging and Low Resolution Integrated Spectroscopy (OSIRIS) camera spectrograph (Cepa et al. 2000; Cepa 2010). It consists of a mosaic of two Marconi CCD detectors, each with  $2048 \times 4096$  pixels and a total field of view of  $7.8 \times 7.8$  arcmin<sup>2</sup>, providing a plate scale of  $0''.127$  pixel<sup>-1</sup>. To increase the S/N, we used  $2 \times 2$  binning and the standard operation mode with a readout speed of 200 kHz (gain  $0.95$  e<sup>-</sup> ADU<sup>-1</sup>, readout noise  $4.5$  e<sup>-</sup>).

In 2017, we observed Didymos on February 25 from 00:26 to 06:00 UT. A series of images of 180 s exposure time were obtained using the Sloan *r'* filter with the telescope tracking on the asteroid. The observations were run during dark time, with

clear skies and at elevations  $>30^\circ$  and a seeing that varied from  $0''.9$  to  $1''.4$ . In the 2019 apparition, observations were carried out on 3 consecutive nights: March 9, 10, and 11. The observational strategy consisted of identifying the asteroid in the field and placing it in one of the extremes of the CCD, so the images were acquired sequentially and with sidereal tracking while the asteroid was crossing the detector. (Didymos had a differential rate of about  $1'$  hr<sup>-1</sup>; thus, the same field was imaged for the entire nightly run.) The Sloan *r'* filter was used, and the exposure time was fixed to 90 s. The average seeing varied between  $1''$  and  $2''.5$ , depending on the object airmass and atmosphere variation. The asteroid was observed during dark time and with clear skies. On average, the object was observed when it had a local elevation  $>35^\circ$ , i.e., from  $\sim 22:20$  UT to  $\sim 05:10$  UT, with the exception of the second night, 2019 March 10, when a high-speed wind prevented observations until 02:10 UT.

The data reduction was performed using IRAF v2.16 processing packages (Tody 1986, 1993). The APPHOT was used to perform the photometry. The APPHOT is a part of the NOAO.DIGIPHOT package, and it includes tools to locate and compute the center of the sources, fit the sky, and perform aperture photometry. Photometry of the 2017 data was performed with a fixed photometric aperture of radius  $2''.7$ , with the relative calibration between frames calculated using a set of between nine and 24 field stars (depending on how many of a selected subset of bright and well-isolated nearby stars were visible in each frame as the telescope tracked the asteroid). For the 2019 observations where the field did not change during each nightly run, the following steps were performed for each night's data. First, the asteroid was identified in the first and last images. These two points were fitted with a straight line, and an approximate position of Didymos was calculated with the interpolation on each individual image. Second, the PHOT task was applied to each image for retrieving the corresponding magnitude. Three apertures with 7, 8, and 9 pixel radii were used. The same procedure was applied for nine reference stars in the field, which were selected to have a brightness similar to the asteroid. To compute the differential magnitudes of the asteroid, the reference stars were monitored against their median to remove possible variable ones (this procedure was repeated several times). The final differential magnitude was computed as the difference between the median of the best reference stars and the asteroid magnitude. The reported differential magnitudes represent the median values of the magnitudes computed using all three apertures. All of the data points were carefully checked, and those affected by background sources were removed (they were about 5% of all points). The photometric errors were estimated by considering the dispersion of points acquired within short time intervals (3–5 minutes). The median values of these are 0.008, 0.009, and 0.011 mag for the 2019 March 9, 10, and 11 runs, respectively.

### 2.4. Multiple Mirror Telescope

We obtained observations using the Multiple Mirror Telescope (MMT) Observatory 6.5 m on Mt. Hopkins, south of Tucson, Arizona, on 2017 February 25, 2017 March 6, and 2019 March 2. Only the data from 2017 February 25 were of sufficient quality for use and are described here. The seeing was excellent on that night, which turned out to be critical. We obtained 144 images of 100 s each using the MMT CAM and a

Sloan Digital Sky Survey (SDSS)  $r$  filter. The detector is a  $2048 \times 2048$  pixel back-illuminated CCD with a field of view of  $2'.7 \times 2'.7$ . The images were  $1024 \times 1024$  pixels, having been binned on the chip  $2 \times 2$ . The resulting resolution was  $0''.16 \text{ pixel}^{-1}$ . The telescope was tracking the asteroid, but very little trailing was apparent for the star images. The field was dithered by about  $20''$  in R.A. and decl. about every 30 minutes and rotated by  $90^\circ$  halfway through the night. Sufficient field stars were available and could be linked through the night. The sky flats were determined to not be sufficient, so a median flat was constructed from the images. We used the standard aperture photometry routines in IRAF with an aperture of 6 pixel radius. The sky annulus had an inner radius of 12 pixels and was 6 pixels wide, and outliers were removed using a  $3\sigma$  clipping algorithm. The sky value was computed as the centroid of the distribution after bad pixels were removed. (We note that the sky value computation converged quickly, and it appeared adequate for these data. The chip is very uniform, and only removal of cosmic rays from the sky pixel distribution was needed to obtain good relative photometry.) We determined relative magnitudes with the normalized average of the best two field stars at any given time. The chosen stars were as bright or slightly brighter than Didymos ( $V = 19.3\text{--}21.5$ ). The formal uncertainties range from 0.024 to 0.045 mag, and we adopt a standard deviation of 0.032 mag for the instrumental magnitudes. This is the unweighted standard deviation of all of the measurements.

### 2.5. William Herschel Telescope

Observations were obtained on the night of 2017 March 31 using the ACAM imager on the 4.2 m William Herschel Telescope (WHT). The ACAM is mounted at the Cassegrain focus and has a circular field of view of diameter  $8'.3$  with a pixel scale of  $0''.25 \text{ pixel}^{-1}$ . Light curves were obtained in the Sloan  $r$  filter, with occasional frames taken with the Sloan  $g$  filter to ascertain the colors of Didymos and comparison stars. The exposure time was 180 s for all frames. The telescope tracking was set at half the asteroid rate of motion in an attempt to produce equivalent point-spread functions (PSFs) for Didymos and comparison stars. Image processing and calibration was performed using AstroImageJ (Collins et al. 2017).

The night was nonphotometric with variable cirrus. Variations in transmission were typically in the range of 0–0.3 mag but occasionally exceeded 1 mag for a period of several frames. Seeing varied during the night from  $\sim 0''.8$  to  $\sim 1''.3$ . With the telescope tracked at half the asteroid rate of motion, the stellar and asteroid images had a fairly constant equivalent FWHM of  $\sim 6$  pixels ( $1''.5$ ). However, several frames were trailed due to a lost autoguider signal, and it became apparent that the actual tracking was not accurate enough to ensure consistent PSFs between the stars and the asteroid, precluding the use of small-aperture radii for photometry. Multiaperture tests indicated an optimal choice of 10 pixel radius ( $2''.5$ ).

A test for differential extinction using the relative colors of field stars showed no detectable effect, so all unsaturated field stars at least 2 mag brighter than Didymos that were within the field for at least half the night were used for calibration. None of the 12 suitable stars showed relative variability. For any given frame, seven to nine stars were typically observed and used to construct a synthetic comparison star. The resultant uncertainties in the synthetic star instrumental magnitudes were generally  $\sim 0.001$  mag and always less than 0.003 mag. The

overall uncertainties are dominated by Didymos photon noise and background subtraction.

Images were removed from the sequence for a variety of reasons: close proximity to background stars, trailed images, a cosmic ray superimposed on the asteroid image, and cloud extinction causing uncertainties greater than 0.045 mag. Of the 166  $r$  frames obtained, 100 were used in the light-curve analysis (Section 3).

Using PS1 catalog magnitudes for the field stars, we determined color terms for the ACAM system and derived a Didymos color of  $(g - r)_{\text{PS1}} = 0.52 \pm 0.04$  and a mean magnitude of  $r_{\text{PS1}} = 18.23 \pm 0.01$ . Using transformation coefficients from Tonry et al. (2012), we derive a mean Johnson  $V$  magnitude of  $18.48 \pm 0.02$ .

### 2.6. New Technology Telescope

Observations with the 3.6 m ESO New Technology Telescope (NTT) were performed using the EFOSC2 instrument (Buzzoni et al. 1984), which provides a  $4'.1$  field of view and  $0''.24$  pixels in a  $2 \times 2$  binned readout (Snodgrass et al. 2008). Two runs were performed in 2017 April, both in visitor mode. Seventy-nine exposures were taken on the night of 2017 April 2, with 300 s exposure times. Conditions were good, but unfortunately, Didymos was near a faint star during the mutual event that night, and the data are not used in the rest of the analysis. Over 3 consecutive nights from April 24, 162 exposures were taken, with the useful data being the 108 frames acquired on the last night, April 27, with seeing around  $0''.7$  FWHM (conditions on the first 2 nights were poor, and limited data were collected). Images were taken through an SDSS  $r$ -band filter with exposure times of 180 s and the telescope tracking at half the asteroid's nonsidereal rate. Data reduction and photometry were performed using IRAF tasks; the photometry was calibrated against field stars from the PS1 catalog.

### 2.7. Gemini North Telescope

Observations of Didymos were obtained with the 8.1 m Gemini North Telescope in Hawai'i using the Gemini Multi-Object Spectrograph (GMOS; Hook et al. 2004) in imaging mode on the nights of 2017 May 4, 2020 December 12, 2021 January 12, and 2021 January 17. In all cases, the Sloan  $i'$  filter was used to maximize throughput given the redder-than-solar color  $(V - I) = 0.82$  of Didymos (Kitazato et al. 2004). The GMOS has a  $5'.5$  square field of view and, with  $2 \times 2$  binning, a pixel scale of  $0''.16 \text{ pixel}^{-1}$ .

For the night of 2017 May 4, the telescope was tracked at Didymos rates of motion, and exposure times of 200 s were used. The night was photometric, and the seeing varied between  $\sim 0''.5$  and  $\sim 0''.7$ . The data were reduced using standard methods with the Gemini IRAF package.<sup>24</sup> Differential aperture photometry was performed with AstroPy 2.0.2 (Astropy Collaboration et al. 2018) and its affiliated package PhotUtils 0.4 (Bradley et al. 2017). Elliptical apertures were used for the nine trailed SDSS reference stars. Tests with multiple apertures indicated an optimal S/N with an aperture of radius 1.5 FWHM of the PSF. The final light curve was an average of the differential photometry calculated with the two closest (and most stable) reference stars. A median light curve

<sup>24</sup> <https://ui.adsabs.harvard.edu/abs/2016ascl.soft08006G>

using all nine reference stars was noisier due to the fact that most of them were also fainter than the two closest reference stars.

On 2020 December 12, 2021 January 12, and 2021 January 17, a sequence of observations was executed for a duration of 4.1, 4.5, and 6.1 hr, respectively, corresponding to 141, 183, and 240 images in turn. (Observations taken on 2020 December 10 were not usable due to a pointing error.) The final number of usable data points was 89, 107, and 142, respectively; a significant fraction of the data points were removed during the reduction process, as they were affected by less ideal sky conditions, interference with background sources, or other observational issues. Exposure times of 70 s were used in December and 50 s in January, as the object brightened from  $V = 20.0$  to 19.5. The telescope tracking was set to sidereal, while the telescope was repositioned every hour to keep the target centered on the CCD chip. The sky brightness was 50th percentile, while the weather constraints were 70th percentile cloud cover and 85th percentile image quality.<sup>25</sup>

We carried out four independent methods of data reduction and analysis for the 2020 December and 2021 January observations. We determined the approach which started by making use of Theli3<sup>26</sup> (Schirmer 2013) provided the best results. We began by visually inspecting the portable network graphics format images enhanced following the method described in Chandler et al. (2018). We noted significant guide probe interference on 2020 December 12 and identified potential photometric contaminants (e.g., cosmic rays, background source blending) in 149 of the 564 images of Didymos. Making use of the Theli3 software package, we executed a series of data reduction steps, including overscan correction, bias subtraction, flattening of fields, background correction, and collapse correction. We conducted astrometry and embedded updated World Coordinate System (WCS) with Theli3 and/or AstrometryNet (Lang et al. 2010) or PhotometryPipeline (Mommert 2017). Both Theli3 and PhotometryPipeline query the Vizier catalog service (Ochsenbein et al. 2000). The catalogs we queried were the SDSS Data Release 9 (Ahn et al. 2012), Gaia Data Release 2 (Gaia Collaboration et al. 2018), and Gaia Early Data Release 3 (Gaia Collaboration et al. 2021). Following Chandler et al. (2018), we extracted thumbnail images of Didymos to check for any additional image artifacts and confirm WCS validity. The final version of photometry we produced made use of PhotometryPipeline. We note that while it would be ideal to limit photometric calibration to field stars with similar colors to those of Didymos ( $U - B = 0.211 \pm 0.032$ ,  $B - V = 0.795 \pm 0.016$ ,  $V - R = 0.458 \pm 0.009$ , and  $V - I = 0.820 \pm 0.009$ ; Kitazato et al. 2004), there were insufficient field stars available. We selected the PS1 photometry (Tonry et al. 2012) because of the availability of calibration stars. We manually checked the photometry with the Aperture Photometry Tool (Laher et al. 2012) on a case-by-case basis. We also used the catalog tool within DS9 to check the reference star photometry.

## 2.8. Magellan Telescope

Observations were obtained with the Baade Magellan 6.5 m telescope at Las Campanas in Chile on 2019 February 2. This was a follow-up to the observations with DCT on 2019 January 31; we needed to complete the coverage of Didymos’s primary

<sup>25</sup> See <http://www.gemini.edu/observing/telescopes-and-sites/sites> for an explanation of the use of percentiles for the Gemini weather conditions.

<sup>26</sup> <https://github.com/schirmermischa/THELI>

light curve with the additional observations to obtain a robust light-curve decomposition on this epoch. We used the WB4800-7800 very broadband VR filter that covers the wavelengths between 480 and 780 nm to maximize the S/N of Didymos. Didymos was imaged over about 80 minutes using 120 s images in photometric conditions with  $0''.85$  seeing using the IMACS imager, which has a pixel scale of  $0''.2$ . The photometry extraction was performed using the PhotometryPipeline described in Section 2.1. The photometry was calibrated to the PS1 catalog in the  $r$  band using stars near Didymos in the science images.

## 2.9. Keck Telescope

Observations were made with the Low Resolution Imaging Spectrometer (LRIS) instrument in its imaging mode using the Atmospheric Dispersion Corrector at Keck I on 2021 January 14 from 11:20 to 16:09 UT. The LRIS includes both a “blue” and a “red” side, with simultaneous images obtained on both sides with different filters. Here we present only red-side data analysis; blue-side images are not included in this work. The LRIS  $R$  filter has an effective wavelength of 642 nm and FWHM of 119 nm.<sup>27</sup> The  $R$ -filter images of Didymos were obtained with 120 s exposure times. Sidereal tracking was used, with the asteroid allowed to move across the field of view. The red side of LRIS has a plate scale of  $0''.123 \text{ pixel}^{-1}$ . Data reduction was done using the standard techniques provided in IRAF (Tody 1986), with extraction of magnitudes using the aperture photometry `apphot` routines.

Four unsaturated stars in the field with Didymos with a range of brightnesses were identified in the SDSS (Blanton et al. 2017; Ahumada et al. 2020) and used as on-chip standards. On-chip standard stars were selected via the SDSS online Skyserver query database, which included data up through SDSS Data Release 16 (Ahumada et al. 2020). Data Release 16 is part of SDSS-IV (Blanton et al. 2017). Three of the stars were used to calculate Didymos’s magnitude; the fourth (which was of a brightness similar to Didymos’s) was used as a comparison and control. No filter transformation was calculated between the published SDSS magnitude and the Keck  $R$ -filter magnitude. The average magnitude uncertainty for Didymos and the control star on an image was typically  $<0.01$  mag. While 94 images were obtained, several of the later images were compromised by twilight and rejected. In addition, close passes to stars by Didymos as it moved in the sky and occasional unlucky-placed cosmic-ray strikes compromised some measurements. A total of 69 images remained for inclusion in the light curve, covering the period of 11:20–15:43 UT. Apertures with diameters of 12 pixels (roughly  $1''.5$ ) were used in extraction.

## 2.10. Large Binocular Telescope

We obtained observations using the Large Binocular Telescope (LBT) on 2021 January 18 and the MODS1 and MODS2 cameras, each with a  $v$  and  $r$  filter, with a plate scale of  $0''.12 \text{ pixel}^{-1}$ . MODS1 and MODS2 are Multi-Object Double CCD Spectrographs/Imagers. The field of view is  $6' \times 6'$  and consists of a  $3k \times 3k$  image. We used these images without binning. The images from MODS2 were better, so the  $v$  and  $r$  filter images were shifted and combined into a single data set. We obtained 150 images of 60 s exposures between 08:00 and

<sup>27</sup> <https://www2.keck.hawaii.edu/inst/lris/filters.html>

10:58 UT. The telescope was tracking the asteroid, and slight trailing was apparent in the stars. The detector is made up of several chips with offset background levels and one to two bad columns at the edges. The asteroid was kept away from the edges, but the comparison stars did move from one region to another. We used the three best comparison stars to obtain the differential magnitudes and linked frames where the comparison stars changed. The comparison stars were at or somewhat brighter than Didymos ( $V = 16.8\text{--}19.3$ ). We used the standard aperture photometry routines in IRAF with an aperture with a 10 pixel radius. The sky annulus used was at a radius of 13 pixels and was 6 pixels wide, and outliers were removed using a  $3\sigma$  clipping algorithm. The formal uncertainties are 0.004–0.007 mag, and the estimated repeatability of the data is 0.009 mag. We measured the rms value of the comparison star data over short enough time intervals that the signal was constant in order to determine the repeatability level.

### 2.11. Telescopio Nazionale Galileo

Telescopio Nazionale Galileo (TNG) is operated on the island of La Palma by the Centro Galileo Galilei of the Istituto Nazionale di Astrofisica (INAF) at the Spanish Observatorio del Roque de los Muchachos of the Instituto de Astrofísica de Canarias. The TNG images of Didymos were obtained on 2021 January 20 with the Device Optimised for the LOw RESolution (DOLORES) instrument. The detector is a  $2048 \times 2048$  E2V 4240 thinned, back-illuminated, deep-depleted, Astro-BB coated CCD with a pixel size of  $13.5 \mu\text{m}$ . The scale is  $0''.252 \text{ pixel}^{-1}$ . The instrument was equipped with the broad-band  $R$  filter of the Johnson–Cousins system.<sup>28</sup> Didymos was observed with the telescope tracked at half its apparent (nonsidereal) motion. More than 300 images were acquired consecutively, starting at 2021 January 20 00:15:30 UTC, with a single exposure time of 60 s for most of the images and  $2 \times 2$  binning.

Standard dome and sky flats did not prove themselves effective in correcting the field illumination. For this reason, a “superflat” was made by averaging the scientific images after masking the sources with the MAKEMASK IRAF package, obtaining a flat-field correction better than the 1% level. On each image, a preliminary WCS solution was obtained by means of the `astroquery` python module<sup>29</sup> from the web service Astrometry.net<sup>30</sup> that provided a robust blind WCS solution. Then, optimal aperture photometry was performed with the `MAG_AUTO` routine of `SExtractor` (Bertin & Arnouts 1996) on the whole field covered by each image. The final WCS solution was obtained with `Scamp` (Bertin 2006), comparing the preliminary WCS positions of the stars in the field with the Gaia eDR3 catalog, and Didymos was recognized in the field by querying the JPL catalog with the `jplhorizons` python module,<sup>31</sup> cross-matching the measured Didymos positions on each image with the JPL ephemerides, by means of the `Stilts` code (Taylor 2006).

To build Didymos’s light curve, a set of 25 bright (nonsaturated) reference stars was chosen on a reference image, collected in the middle of the run, with a typical

photometric uncertainty better than 0.02 mag. The maximum relative offset of the other images, because of the motion of Didymos, was on the order of  $\pm 100$  pixels in both axes. The positions of the reference stars were cross-matched between the reference and the other images with the `DAOMATCH/DAOMASTER` code (Stetson 1993), resulting in a minimum overlap of 14 stars in the worst case. `DAOMATCH/DAOMASTER` also computes the photometric offset between the reference and the other images, with a robust weighted mean that discards the outliers and delivers a catalog where all the measurements are photometrically aligned to the catalog of the reference image. Computed offsets were added to the Didymos individual measurements, obtaining a homogeneous light curve in the reference image system. After discarding several outliers (due to contamination of the Didymos image by nearby sources, hot pixels, or other effects), we ended up with 296 data points. The robustness of our procedure was tested by choosing a few isolated stars in the field of brightness similar to Didymos and not among the reference stars, obtaining for each of them a flat light curve within the uncertainties. The median of the photometric errors of the individual data points calculated by `SExtractor` was 0.011 mag, but the real errors were greater (see Section 3), as the noise model in `SExtractor` does not account for all noise sources.<sup>32</sup> Finally, the absolute calibration was obtained by selecting, among the 25 reference stars, 11 stars with good SDSS  $g'$ ,  $r'$  measurements and then transformed to Johnson  $R$  magnitudes by means of the transformations published in Lupton et al. (2005).<sup>33</sup> We estimate the uncertainty of the calibration to be 0.019 mag.

## 3. Light-curve Decompositions

The light curve of a binary asteroid generally consists of three components: the primary rotation light curve, the secondary rotation light curve, and the mutual event (orbital) light curve. The primary rotation light curve is always apparent (with observations of sufficient accuracy), while the secondary rotation light curve may or may not be resolved depending on the secondary-to-primary size ratio, elongation of the secondary, and accuracy of the photometric observations. When the binary asteroid is in a mutual occultation or eclipse geometry, i.e., when Earth or the Sun, respectively, is close to the mutual orbit plane of the two bodies, then there are superimposed brightness attenuations due to the occultations or eclipses (collectively called “mutual events”) that occur between the two bodies as they orbit one another. For analysis and modeling of the photometric data of a binary asteroid, we decompose its light curve using the method of Pravec et al. (2006), which we briefly outline in the following.

The binary asteroid light curve outside mutual events, consisting of the two rotational light curves, can be represented as a linear addition of two Fourier series,

$$F(t) = F_1(t) + F_2(t), \quad (1)$$

$$F_1(t) = C_1 + \sum_{k=1}^{m_1} \left[ C_{1k} \cos \frac{2\pi k}{P_1}(t - t_0) + S_{1k} \sin \frac{2\pi k}{P_1}(t - t_0) \right], \quad (2)$$

<sup>28</sup> <http://www.tng.iac.es/instruments/filters/>

<sup>29</sup> [https://astroquery.readthedocs.io/en/latest/astrometry\\_net/astrometry\\_net.html](https://astroquery.readthedocs.io/en/latest/astrometry_net/astrometry_net.html)

<sup>30</sup> <https://astrometry.net/>

<sup>31</sup> <https://astroquery.readthedocs.io/en/latest/jplhorizons/jplhorizons.html>

<sup>32</sup> <https://sextractor.readthedocs.io/en/latest/Photom.html>

<sup>33</sup> See also <https://www.sdss.org/dr12/algorithms/sdssubvritransform/>.



$$F_2(t) = C_2 + \sum_{k=1}^{m_2} \left[ C_{2k} \cos \frac{2\pi k}{P_2} (t - t_0) + S_{2k} \sin \frac{2\pi k}{P_2} (t - t_0) \right]. \quad (3)$$

where  $F(t)$  is the total light flux at time  $t$ ,  $F_j(t)$  are the light fluxes of the components at time  $t$ ,  $C_j$  are the mean light fluxes of the components,  $C_{jk}$  and  $S_{jk}$  are the Fourier coefficients,  $P_j$  are the rotation light-curve periods,  $t_0$  is the zero-point time, and  $m_j$  are the maximum significant orders (see also Pravec et al. 2000 and references therein). (We designate quantities belonging to the primary and secondary with the indices “1” and “2,” respectively.) The two constant terms add to  $C_0 = C_1 + C_2$ , which is fitted in analysis. We note that the two rotational light curves can be taken as additive in the combined binary asteroid light curve if the effect of mutual illumination between the two bodies is negligible. We further note that using the representations of Equations (2) and (3), we assume principal axis rotation for each component; nonprincipal axis rotation would produce a complex light curve. (The light curve of an asteroid in the state of free precession can be represented with a two-period Fourier series, see Pravec et al. 2006, but it might not be a good representation for a more complex or chaotic rotation of the component of an unrelated binary asteroid system.) The maximum significant orders  $m_j$  of the fitted Fourier series are determined from the significance F-test (see, e.g., Magnusson et al. 1995). We note that the decomposition of a binary asteroid light curve into the primary and secondary light curves with Equations (2) and (3) is a well-constrained problem, and a unique solution is obtained with photometric data of sufficient amount and quality unless the periods  $P_1$  and  $P_2$  are close one other or commensurate (which is not the case for Didymos).

Using the representation for binary asteroid rotational light curves above implicitly assumes that the two rotational light curves are constant; i.e., neither the Fourier coefficients nor the rotation light-curve periods change with time. (The light-curve data must also be reduced to unit geo- and heliocentric distances and a consistent solar phase, e.g., using the  $H$ - $G$  phase relation, to correct for the flux changing inversely proportional with the square of the distances and with the phase function. The times were reduced for light-travel time; i.e., we work in the asteroid-centric frame.) In reality, the rotational light curves are not constant, as the Earth-asteroid-Sun viewing and illumination geometry changes with time, and the synodic rotational light-curve periods are not constant due to the varying apparent angular rate of the asteroid. (The synodic-sidereal rotation period difference can be approximated using the phase angle-bisector formalism; see, e.g., Pravec et al. 1996.) However, the rotational light-curve shape and period changes are usually small over short time intervals, so their representation with Equations (2) and (3) can be used if we combine light-curve data taken on nearby nights.

As will be shown below, observable changes of the Didymos primary rotational light curve occurred on timescales from a couple of days to a couple of weeks (depending on the specific Earth-asteroid-Sun geometry at individual epochs). The light-curve data taken over longer time intervals therefore had to be analyzed and decomposed separately.

Changes of the synodic primary rotation period due to the changing apparent angular rate of Didymos were generally

small, on an order of a few 0.0001 hr. They were entirely negligible over the short time intervals (which were not longer than a couple weeks) of the individual Didymos light-curve decompositions presented below, and they were also small over the course of the individual apparitions (though the estimated mean synodic periods differed slightly between the individual apparitions).

In fitting the rotational light-curve data with the Fourier series, observations taken outside mutual events are used. Data points covering mutual events are therefore masked at this stage. As the beginning and end of a mutual event are generally sharp light-curve features, the data points taken in mutual events can usually be easily identified, and they are masked iteratively while refining the Fourier series fit in a few steps. (While the rotational light curves are generally smooth and therefore can be represented with the Fourier series cut at relatively low orders, the brightness attenuations caused by mutual events begin and end abruptly as the two bodies start and finish transiting one another with respect to Earth or the Sun.) When we are uncertain if a particular data point near the beginning or end of a mutual event is inside or outside the event, it is usually better to be conservative and mask it as well; we typically get enough data points outside events to define the rotational light curves, even in the case where we mask out a few more points near the beginning or end of an event.

When combining photometric data taken with different telescopes or on different nights, which was the case for most of the Didymos data (see below), we took the data sets obtained from different telescopes or nights as being on relative magnitude scales to each other. Though some of the data were absolutely calibrated in specific photometric systems with uncertainties of about 0.02 mag, that was generally not accurate enough for our purpose, and we took the zero-points of the magnitude scales of the individual observing runs as free parameters in the Fourier series fits.

Finally, we note that the observations of Didymos taken with different telescopes or by different teams were made in a few different filters (though most of the detector+filter combinations had a peak response at red wavelengths). The combination of light-curve data taken in different filters (at visible wavelengths) is not considered to be a problem for the light-curve analysis, as asteroids do not show large-scale color nonuniformities, so the light curves measured in different filters are expected to look the same. Nevertheless, in the light-curve decompositions presented below, we paid attention to the possible systematic differences between data from different telescopes that might be attributable to a large-scale color difference, but we did not find any.

We applied the light-curve decomposition method outlined above to the obtained Didymos photometric data from the five apparitions presented in Section 2. We present the light-curve decomposition data in Table 2 and the figures referenced there. We have obtained the light-curve decompositions for data taken during 16 separate intervals (including the three presented in Pravec et al. 2006), with the primary rotation light-curve shape appearing constant during each of the individual intervals. In the table, the first column gives the observational interval used for the individual decomposition, with the subsequent columns giving the total number of photometric data points used, the number of events covered (at least partially) by the observations, the rms residual of the best Fourier series fit to the rotational light-curve data outside the

events (it was converted from light flux units to magnitudes using  $\delta m = 2.5\delta F/C_0/\ln 10$ ), the solar phase angle ( $\alpha$ ), the true anomaly of Didymos in its heliocentric orbit ( $\nu$ ; these two angles are for the center of the given observational interval), and the reference to a plot of the light-curve decomposition. We note that though we did the fits of the Fourier series (Equations (2) and (3)) in light flux units—i.e., we converted the reduced magnitudes to flux units for the fitting—we then converted the resulting separated light-curve components back to magnitudes for plotting in panels (b) and (c) of the presented figures. (The individual light-curve components plotted in panels (b) and (c) of the figures were obtained from the reduced photometric data by subtracting the variable parts of the other light-curve components, Equations (2) and (3). The constant part  $C_0 = C_1 + C_2$  was kept, and it was not subtracted for the plotting. This is because we do not know a priori, before further modeling that follows the light-curve decomposition, what fraction of the mean light flux of the system ( $C_0$ ) belongs to the primary or secondary.) These plots show how the Didymos light curve would appear if there was only the secondary/orbital light curve (panel (b); corresponding to a case of spheroidal primary) or primary light curve (panel (c); corresponding to a case of spheroidal secondary and the system being outside the mutual event geometry) present. In the figures, the solid curves are the fitted Fourier series (Equation (1)) in panel (a), and the fitted primary rotational light curve (Equation (2), with the constant part  $C_0$  kept, as commented above) in panel (c). The Fourier series coefficients are presented in the [Appendix](#). We comment on the individual light-curve decompositions presented in [Table 2](#) and the figures referenced there in the following.

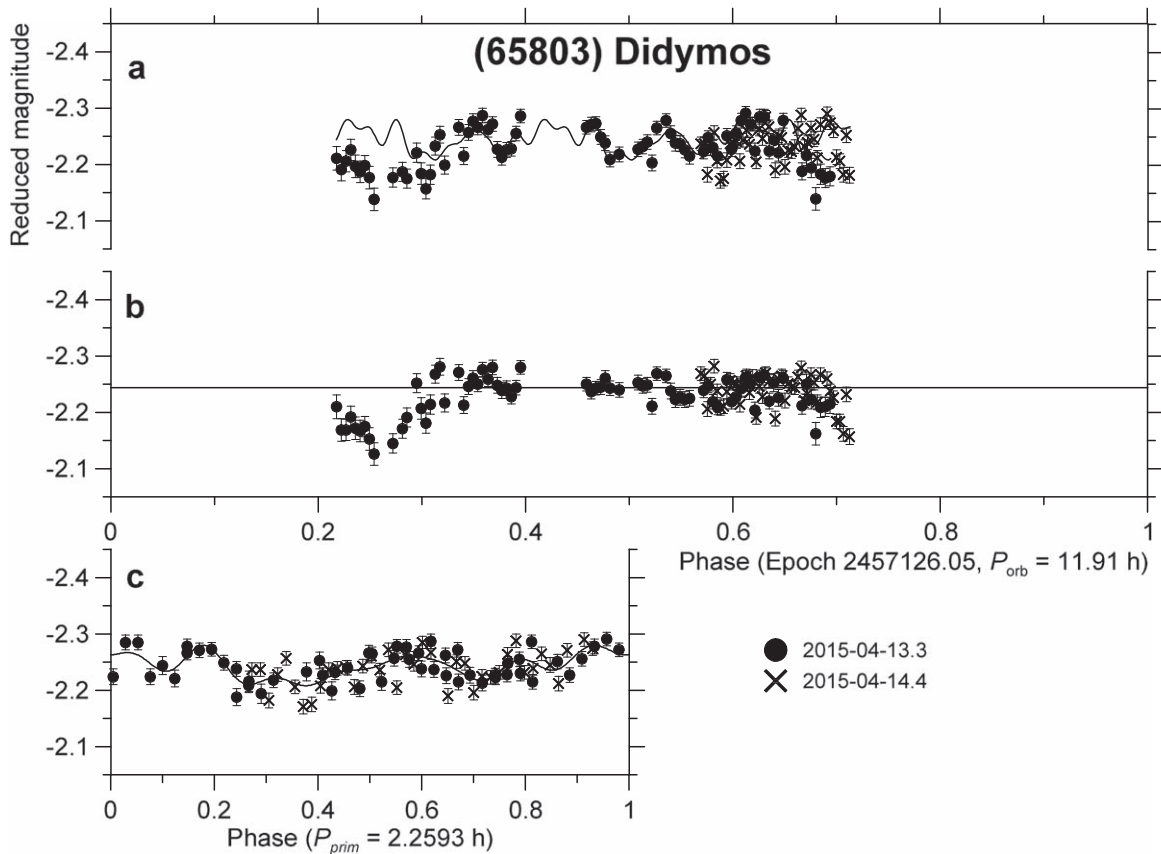
The Didymos photometric data taken in 2003 were analyzed, and their light-curve decompositions were presented in [Pravec et al. \(2006\)](#). The three light-curve decompositions obtained covered intervals 4, 8, and 4 days long; see the first three rows in [Table 2](#). They were high-quality data with rms residuals of the Fourier fits to the rotational light-curve components of 0.008, 0.008, and 0.012 mag, respectively. As many as 18 mutual events were fully or partially covered by the observations. The shapes of the mutual events changed quite rapidly with the changing Earth–asteroid–Sun geometry during the observations taken shortly after the close approach to Earth that occurred on 2003 November 12. The changes were particularly prominent for the primary events (plotted around orbital phase 0.25 in [Figures 1\(b\)–3\(b\)](#) of [Pravec et al. \(2006\)](#)), as they were particularly sensitive to the specific viewing and illumination geometry of the binary system in the observed primary eclipses and occultations. We also note that the observed synodic primary rotation period was 2.2592–2.2593 hr, so this value was used for the light-curve decompositions of the 2003 data, but the synodic–sidereal primary rotation period difference was estimated to be 0.0008 hr; the sidereal primary rotation period was determined to be  $2.2600 \pm 0.0001$  hr in further modeling (see [Naidu et al. 2020](#)). We further note that the synodic orbital period was estimated to be 11.91 hr, and it was used for the light-curve decompositions. (Again, the sidereal orbital period was slightly greater; see [Scheirich & Pravec 2022](#).) Our last comment on the 2003 data is that the data obtained after subtraction of the primary light-curve component did not show a flat (constant) secondary light curve outside mutual events (see [Figures 1\(b\)–3\(b\)](#) of [Pravec et al. \(2006\)](#)). While [Pravec et al. \(2006\)](#) suggested that it might be due to the rotation of a nonspheroidal secondary, we consider the features seen in the 2003 secondary light curves outside mutual

events to be spurious rather than real features produced by the secondary’s rotation (see [Section 4](#)).

The observations taken with DCT on 2015 April 13 and 14 were quite limited (total coverage of 7.4 hr) and relatively noisy, but we were able to decompose them ([Figure 1](#)). For the light-curve decomposition, we assumed the synodic periods observed in 2003. (Possible small differences between the actual synodic periods in 2015 April and those observed in 2003 would be entirely negligible for decomposition of the short 2015 data.) As for the decompositions of the 2003 data in [Pravec et al. \(2006\)](#), we used  $G = 0.20$  by [Kitazato et al. \(2004\)](#) for reduction of the 2015 data (as well as the 2017–2021 data below) with the  $H$ – $G$  phase relation. Despite the relatively high noise of the 2015 data (their rms residual was 0.024 mag), we detected nearly all of one mutual event and a small part of another event (see [Figure 1\(b\)](#)). The primary light curve ([Figure 1\(c\)](#)) was quite complex, with several local extrema; the harmonics up to the eighth were significant ( $m_1 = 8$  in [Equation \(2\)](#)). This multimodal primary light curve, which is markedly different from the primary light curves observed in 2003 ([Figures 1\(c\)–3\(c\)](#) in [Pravec et al. \(2006\)](#)) that were predominated by the first or second harmonic, indicates that there were local topography effects present at the viewing and illumination aspect in 2015 April that were not seen in 2003. (The 2015 observations were taken at a small solar phase angle of  $3^\circ$ , so the observed multimodal primary light-curve shape was not related to a complex shadowing that could be present at high phase angles.) These data may be useful for refining the primary shape model in future.

In 2017, we obtained three light-curve decompositions ([Figures 2–4](#)). They were mostly relatively noisy data again (rms residuals 0.017–0.030 mag), but we were able to decompose them grouped in three intervals that were 6, 2, and 16 days long. (The last interval might seem somewhat long, but we did not see an obvious change of the primary light-curve shape over the 16 days, though it is possible that small changes of the primary light-curve shape were hidden in the noise.) Despite the noise, we detected seven mutual events in full or partially. Like in 2015 April, the primary light curves ([Figures 2\(c\)–4\(c\)](#)) showed multiple extrema. This indicates that the features of local topography that affected the 2015 primary light curve were present during the 2017 observations as well. Indeed, the heliocentric true anomaly of Didymos during the 2017 observations,  $147^\circ$ – $162^\circ$ , was similar to its true anomaly on 2015 April 13–14 ( $168^\circ$ )—Didymos was seen on similar aspects in the two apparitions—but it was quite different from the true anomaly values of  $27^\circ$ – $53^\circ$  of the 2003 observations when we saw the more regular primary light curves. We note that we found that the synodic primary period in this apparition was close to (within the error bars of) the 2.2600 hr sidereal primary period, so we used this period for the 2017 light-curve decompositions. We estimated that the synodic orbital period was 11.917 hr in this apparition; like in 2003, it was somewhat shorter than the sidereal orbital period we found in subsequent Dimorphos orbit modeling.

In 2019, we obtained two light-curve decompositions ([Figures 5 and 6](#)). Unlike the 2015 and 2017 data, the 2019 data were of high quality (we made observing strategy improvements based on experience obtained in 2015 and 2017) with rms residuals of 0.010–0.011 mag. We detected five mutual events partially or in full. We found that the synodic primary and orbital periods in 2019 were close to the values observed in 2017, though we were not able



**Figure 1.** Didymos light curve from 2015 April 13 to 2015 April 14. (a) Data showing all light-curve components, folded with the synodic orbital period. (b) Secondary (orbital) light-curve component, derived after subtraction of the primary light-curve component, showing the mutual events between the components of the binary system. The horizontal line indicates the mean level outside mutual events (corresponding to  $C_0$ ). (c) Primary light-curve component.

to refine them with the short 2019 intervals (both only 2 days long); we used the 2017 synodic period values for the 2019 light-curve decompositions. It is notable that the primary light curves observed in this apparition (Figures 5(c) and 6(c)) were regular again, similar to those observed in 2003 late November and December. Apparently, the local topography features that caused the complex multimodal primary light curves in 2015 and 2017 did not affect it in 2019, when Didymos was seen at lower heliocentric true anomaly values of  $127^\circ$ – $139^\circ$ . We further note that the GTC observations of 2019 March 9–11 showed a nonconstant secondary light curve outside the events; it will be analyzed in Section 4.

The rich data we took in the 2020–2021 apparition allowed us to obtain as many as seven light-curve decompositions (Figures 7–13). They were high-quality data with rms residuals from 0.006 to 0.015 mag. We detected 23 mutual events partially or in full. The synodic primary period was  $2.2602$  hr (formal error  $<0.0001$  hr), as we determined from the highest-quality data obtained from 2020 December 12 to 2021 January 18, and we used this value for all of the light-curve decompositions in this apparition. The synodic orbital period was close to the  $11.917$  hr value observed in 2017, and we used it for all of the 2020–2021 light-curve decompositions. It is particularly interesting that the mutual events were less prominent, mostly shorter and shallower, in this apparition than in all four previously observed apparitions. This was apparent especially between 2021 January 8 and 18 (Figures 8(b)–10(b)), when the primary eclipses, observed around orbital phase 0.29, were short and relatively shallow (with depths about 0.04 mag), and the primary occultations (we have identified the character of the

individual events in Scheirich & Pravec 2022), observed around orbital phase 0.21, were even shallower, especially during January 8–14, when their depth was as low as 0.019 mag (see the depth of the total secondary events,  $0.050 \pm 0.002$  mag, observed on other epochs; see Scheirich & Pravec 2022). Apparently, the Didymos binary system was seen significantly off the mutual orbit plane, i.e., at relatively high angles between its mutual orbit plane and the asteroid–Earth/Sun line (we call them “aspect angles”) that caused the observed occultations/eclipses to be quite off-center and partial. Indeed, as Scheirich & Pravec (2022) found, both aspect angles were near their maximum values in 2021 January, while at least one of them was not close to the extreme on any other epoch in all five observed apparitions. As for the primary light curves (Figures 7(c)–13(c)), they showed multiple extrema in 2020 December and 2021 January again, but it might be a result of observing Didymos at relatively high solar phases ( $26^\circ$ – $44^\circ$ ), where the effects of local topography could be more prominent.

We conclude this section with stating that the photometric data set we obtained for Didymos in the five apparitions during 2003–2021 is among the best obtained for binary near-Earth asteroids so far (comparable only to the data obtained for (66391) 1999 KW4 and (175706) 1996 FG3). Despite the relatively small size of the Didymos secondary ( $D_2/D_1 = 0.21$ ; Scheirich & Pravec 2009), resulting in relatively shallow mutual events, we obtained high-quality data for a good number of mutual events. This required the use of medium- to large-sized telescopes, as Didymos was relatively distant and therefore rather faint during 2015–2021. The obtained mutual

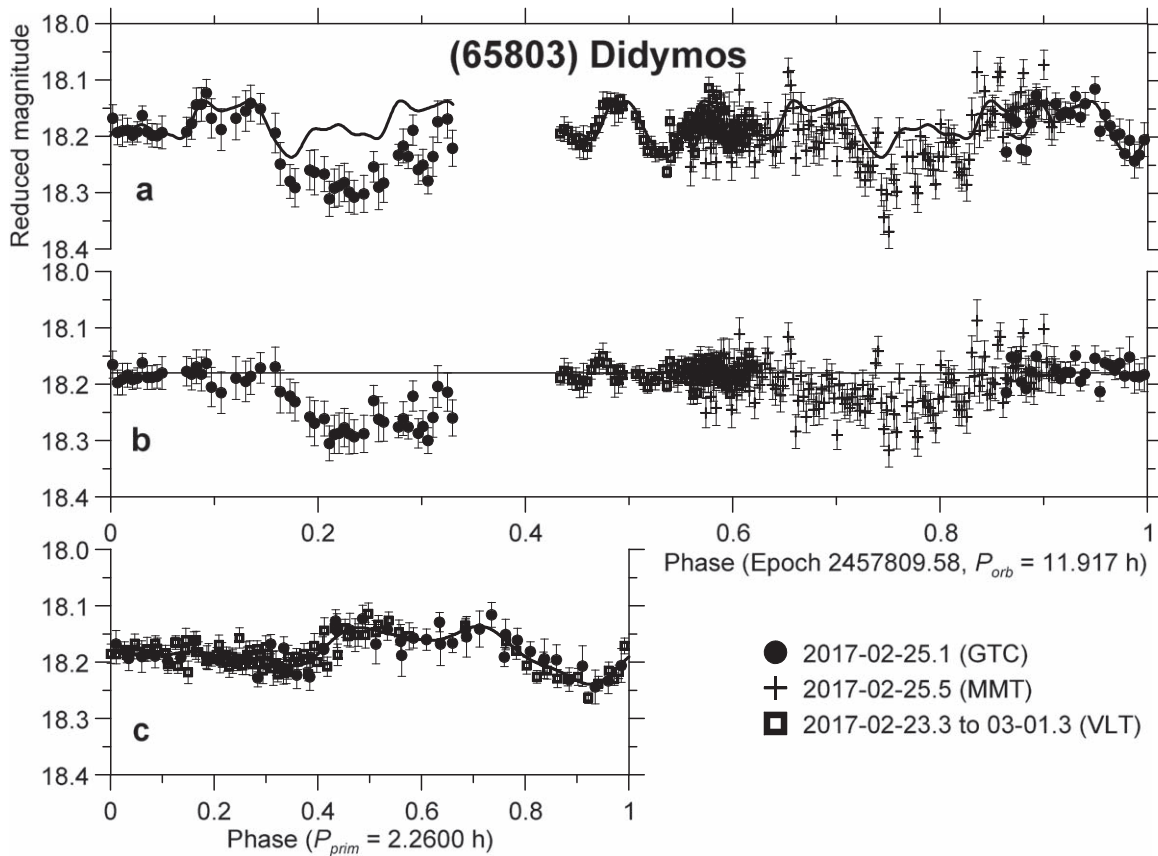


Figure 2. Didymos light curve from 2017 February 23 to 2017 March 1. See the caption of Figure 1 for a description of the content of the panels.

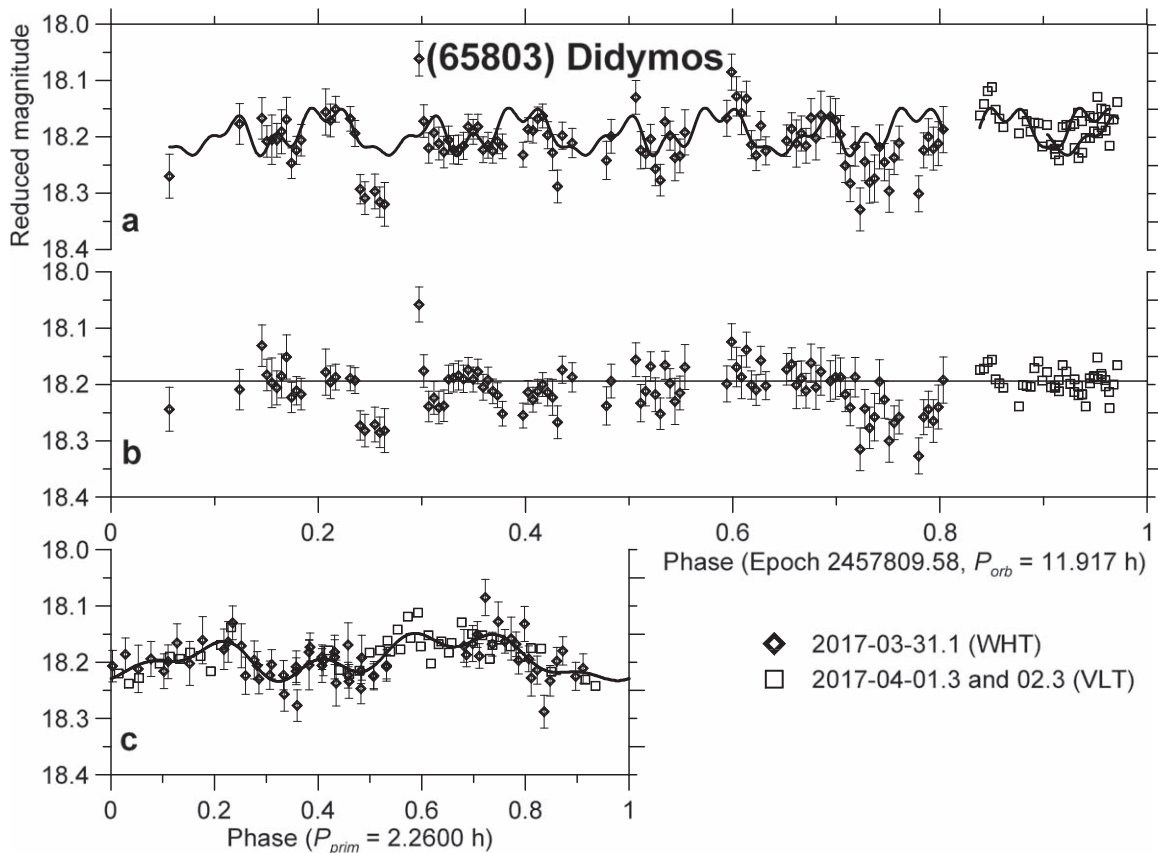
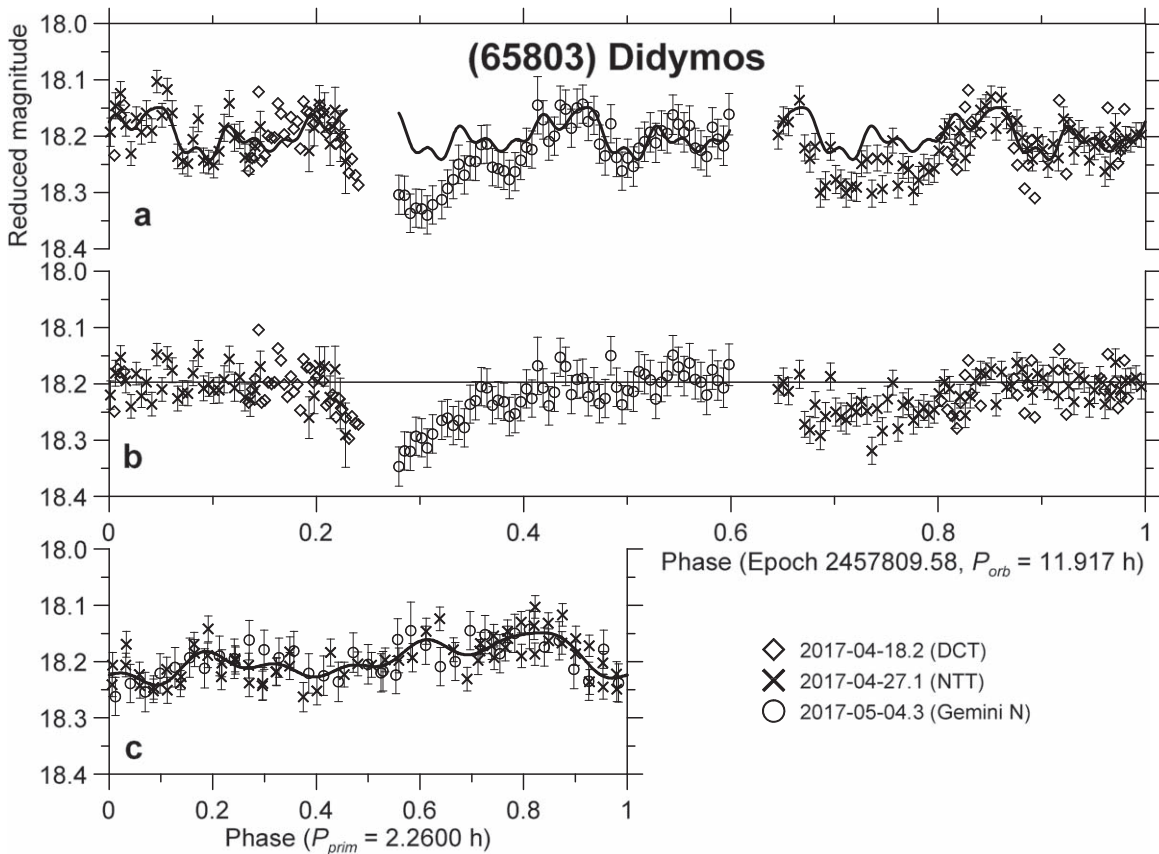


Figure 3. Didymos light curve from 2017 March 31 to 2017 April 2. See the caption of Figure 1 for a description of the content of the panels.



**Figure 4.** Didymos light curve from 2017 April 18 to 2017 May 4. See the caption of Figure 1 for a description of the content of the panels.

event data have been used for modeling the Dimorphos orbit (Naidu et al. 2022; Scheirich & Pravec 2022). The rich experience we have obtained through these observations over five apparitions will be used for performing further high-quality observations before and after the DART impact in the 2022–2023 apparition of Didymos.

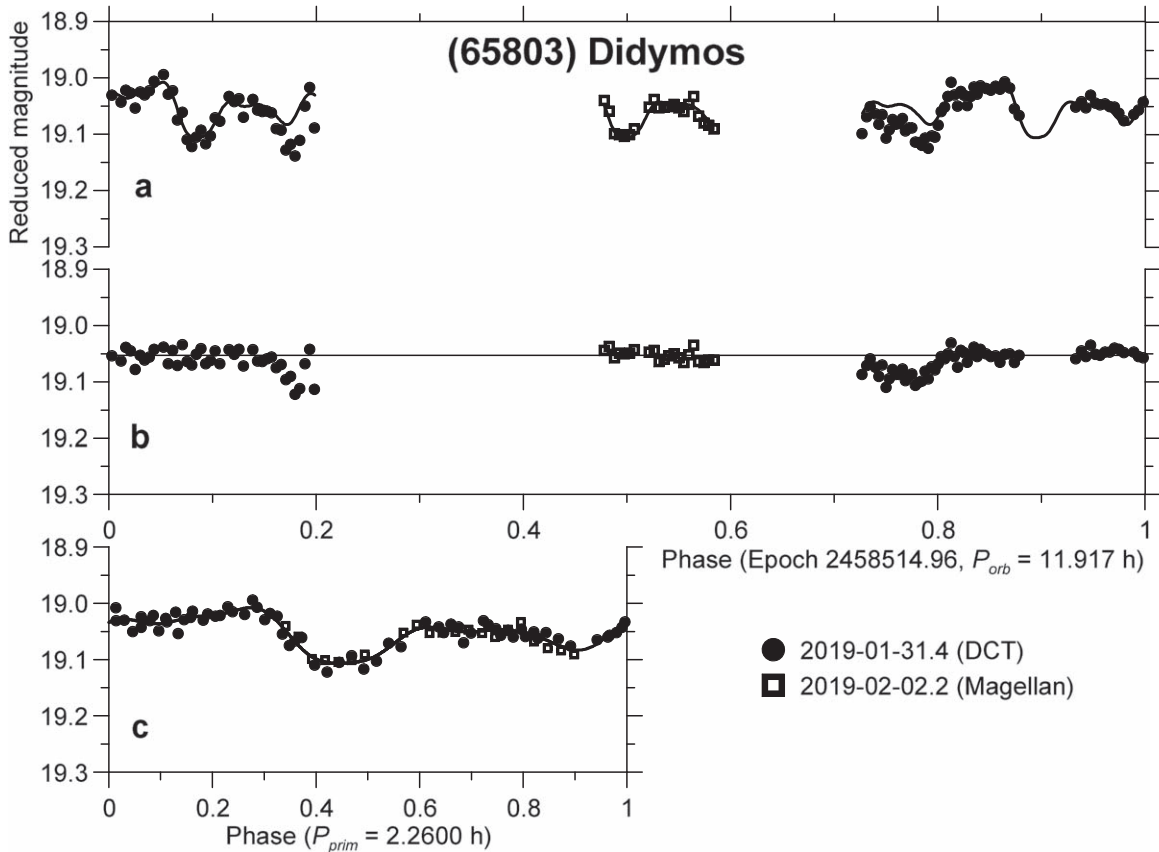
#### 4. Constraints on the Dimorphos Equatorial Elongation

One of the most important parameters of a binary asteroid that can be estimated or constrained from light-curve analysis is the equatorial axis ratio ( $a_2/b_2$ ) of the secondary. Information on the parameter is contained in the amplitude of the secondary light-curve component (Equation (3)). Pravec et al. (2016) analyzed secondary light-curve data for 46 near-Earth and small main-belt asteroids and found that the secondary equatorial elongations have an upper limit of  $a_2/b_2$  of about 1.5. Following this constraint, the DART team has assumed  $a_2/b_2 = 1.3 \pm 0.2$  for Dimorphos. Our preliminary analyses of the Didymos secondary light-curve data in past years revealed that estimating Dimorphos’s equatorial elongation is challenging. This has been because, unlike most binary asteroid secondaries studied in Pravec et al. (2016), the Didymos secondary is relatively small ( $D_2/D_1 = 0.21$ ), so the signal from its rotation is diluted in the light of the much larger primary.<sup>34</sup> That, together with the fact that the observations of Didymos in 2015–2021 were largely optimized for the DART

mission-critical task of precisely determining Dimorphos’s orbit around the primary and not for estimating its elongation, resulted in not yet achieving a conclusive result on Dimorphos’s  $a_2/b_2$ . In this section, we analyze the available data and define the requirements for potential observations optimized for estimating Dimorphos’s elongation in 2022 July–September (before the DART impact).

Pravec et al. (2006) found that their derived Didymos secondary light-curve components were not flat (constant) at orbital phases outside mutual events (see their Figures 1(b)–3(b)). They suggested that the variations seen outside the mutual events might be due to rotation of a nonspheroidal secondary. However, upon further examination of their observations, following more experience that we obtained with observations of binary asteroids since 2006, we more recently suspect that the features seen in the derived 2003 secondary light curves outside mutual events are spurious. We suspect that the apparent variations might be artifacts caused by certain observational issues (such as imperfect flat fields) that they did not have under full control for the fast-moving target in 2003. This suspicion has been strengthened because the apparent features did not look like a rotational light curve of a synchronous secondary (we note that Dimorphos is expected to be in the 1:1 synchronous spin state, as are the secondaries of other well-observed binary asteroids with parameters similar to the Didymos system; Pravec et al. 2016), and they did not repeat consistently over the three observational intervals. Therefore, we suggested that a rotational light curve of the Didymos secondary could be detected with future high-quality observations that would provide photometry consistent at a 0.01 mag (or better) level over several hours covering at least half of the mutual orbit period. This data-quality requirement was set based on the experience obtained

<sup>34</sup> Unlike the case of the binary asteroid secondary, we note that estimating the equatorial elongations of single asteroids with magnitudes similar to Didymos,  $V = 19$ – $20$ , from photometric observations is a routine task (e.g., Throuin et al. 2018).



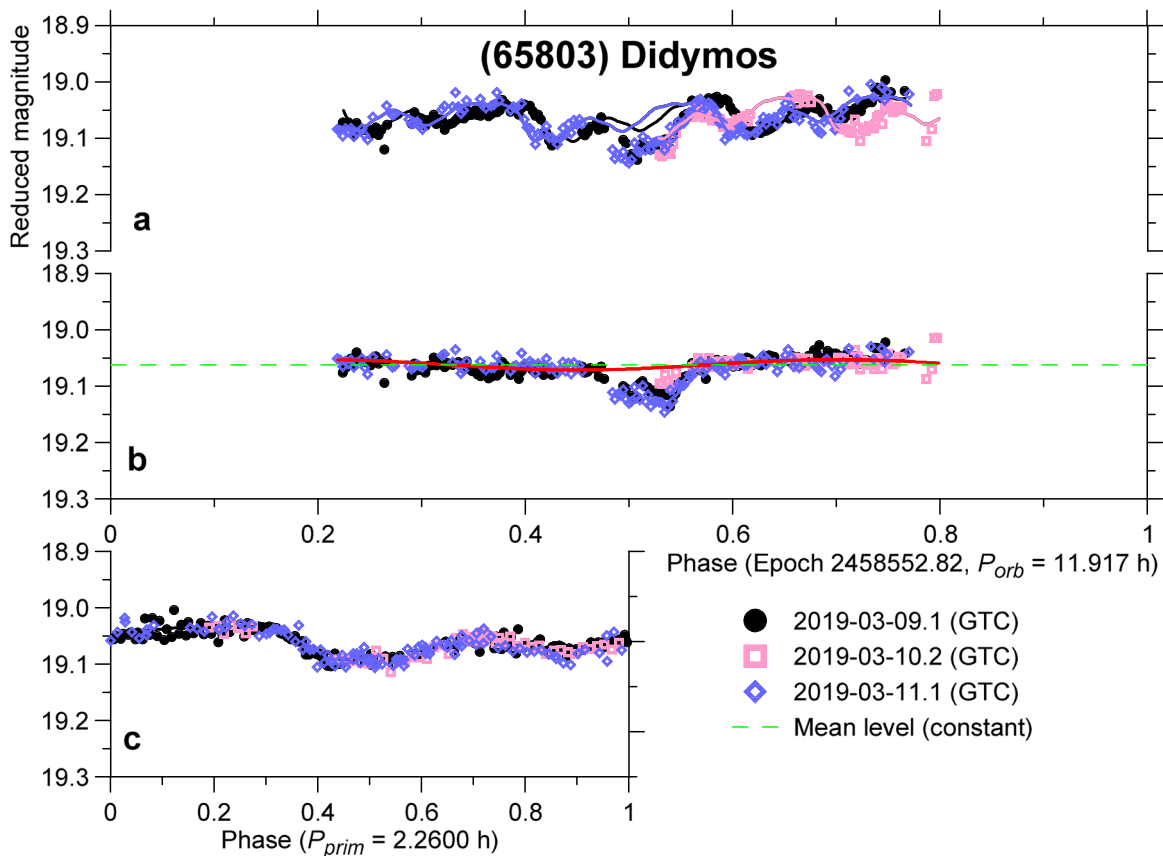
**Figure 5.** Didymos light curve from 2019 January 31 to 2019 February 2. See the caption of Figure 1 for a description of the content of the panels. Note that in this and subsequent figures showing the high-quality data from 2019 and 2020–2021 with errors around 0.01 mag, we do not plot error bars for the individual data points, as they are comparable to the sizes of the data point symbols.

with photometry of other binary asteroids with parameters similar to Didymos (Pravec et al. 2016). In particular, a moderately elongated secondary with  $D_2/D_1 = 0.21$  would produce a secondary light-curve amplitude in the combined primary plus secondary light-curve data not greater than 0.02 mag, hence the need to obtain data consistent at the 0.01 mag level or better.

The photometric observations that we performed in 2015–2021 were mostly of insufficient photometric accuracy or coverage for detecting a rotational light curve of Dimorphos. However, there were a few high-quality and sufficiently long observational runs that allowed us to analyze possible secondary rotational variations outside mutual events.

The data obtained with the LDT on 2019 January 31, 2020 December 23, 2021 January 14, and 2021 March 6, with the third run supplemented with the Keck *R* data of 2021 January 14, were of both high quality (errors about 0.010 mag) and consistent photometric coverage with durations  $\geq 5.6$  hr (i.e., about half of the orbit period), thus suitable for analysis of a possible secondary rotational variation outside mutual events. To check for its possible presence, we fitted the data with the Fourier series (Equation (3)) with the period  $P_2$  set to half of the orbit period and  $m_2 = 1$ . This setting is because the rotational light curve of an elongated synchronous secondary is expected to be predominated by the second harmonic of the orbit period, which corresponds to the first harmonic of half of the orbit period (see Pravec et al. 2016). We found no significant secondary rotational light-curve amplitude in the first, second, and fourth runs; the F-test gave 0.5, 1.1, and 1.6 for them, respectively. The formal  $3\sigma$  upper limits on the

secondary amplitudes in the three runs were 0.013, 0.009, and 0.011 mag, respectively. (We follow the convention in the asteroid research field and report “peak-to-trough” amplitudes of the asteroid light curves.) There was a marginal signal in the secondary light curve of the LDT+Keck run, 2021 January 14; the F-test gave 3.5 for it, with a secondary light-curve amplitude  $A_2 = 0.007$  mag with a formal error of  $\pm 0.002$  mag. Correcting for the mean light from the primary using the formulae in Pravec et al. (2006) gives an estimate for the secondary’s equatorial elongation of  $a_2/b_2 = 1.15$  with a formal error of  $\pm 0.05$ . As the observations were taken at a solar phase angle of  $30^\circ$ , where the secondary light-curve amplitude could be affected by the amplitude-phase effect (Zappalà et al. 1990), it might need to be corrected for that. Using the correction method of Pravec & Harris (2007), we obtained a corrected  $a_2/b_2 = 1.09$ . However, given that we are not sure how exactly the amplitude-phase effect works in the binary asteroid secondary, we suggest adopting the mean of these two values, i.e.,  $a_2/b_2 = 1.12$ . Alternatively, it might perhaps be better to say that we have estimated a formal  $3\sigma$  upper limit on the Dimorphos equatorial axis ratio of 1.30. However, as this exercise was all about analyzing a signal buried in the statistical noise of the observations, we cannot be certain that there were no hidden systematic errors present in the LDT+Keck data on the level of a few 0.001 mag, so we must consider the possibility that there might be some systematic error present in the  $a_2/b_2$  estimate, though we cannot estimate its magnitude at the current stage of our work on the data.



**Figure 6.** Didymos light curve from 2019 March 9 to 2019 March 11. See the caption of Figure 1 for a description of the content of the panels. The data points from the individual nights and the Fourier series (Equation (1)) fitted to them (outside mutual events) are color-coded in this plot (as well as in Figures 7–10); this is to facilitate seeing the quality of the fit to the data outside events in panel (a), where the data from different nights phased with the orbit period heavily overlap. The red curve is the best-fit secondary light curve; see Section 4. Note that the zero-point time (epoch) for this plot was arbitrarily shifted by  $-0.25$  in orbital phase—the observed secondary events are plotted around orbital phase 0.50 and not 0.75, as in all of the other plots—to show the secondary light-curve variation (outside of mutual events) on one continuous plot; it would break at orbital phase 1.0 if we plotted the events around phase 0.75.

The observations taken with GTC on 2019 March 9, 10, and 11, however, showed a different behavior. A formally significant period of 6.05 hr (formal error  $\pm 0.03$  hr) for a monomodal light curve was detected, which corresponds to a bimodal (i.e., predominated by the second harmonic, as expected for an elongated secondary; see above) secondary rotational light curve with a period of 12.10 hr with a formal error of  $\pm 0.06$  hr. This is close but not exactly equal to Dimorphos’s orbital period of 11.92 hr. Assuming that the difference between the two periods of 0.18 hr is not significant (the  $P_2$  formal error of 0.06 hr might be underestimated), we obtained a secondary light-curve amplitude of  $A_2 = 0.017$  mag with a formal error of  $\pm 0.001$  mag assuming  $P_2 = P_{orb} = 11.92$  hr. With the methods mentioned in the previous paragraph, this gave an estimate for  $a_2/b_2 = 1.41$  or 1.37 (the latter after correcting the data for the amplitude-phase effect) with a formal error of  $\pm 0.05$ ; for the reasons mentioned above, we would adopt  $a_2/b_2 = 1.39$ . This is markedly different from the estimate  $a_2/b_2 \approx 1.12$  obtained from the 2021 January 14 LDT+Keck data.<sup>35</sup> Though the formal  $3\sigma$  error bars of the GTC and LDT+Keck estimates overlap (the true  $a_2/b_2$  might thus

perhaps be in the range 1.22–1.30), we feel that it is premature to accept any of the  $a_2/b_2$  estimates that are based on these limited data. In particular, we must consider that the GTC data might be affected by a systematic error over the  $\sim 6.5$  hr long observational runs on the 2019 March 9 and 11 nights. As described in Section 2.3, the asteroid transited over the entire field of view of the GTC’s OSIRIS camera during the 6.5 hr run, so any systematic errors present, e.g., in the flat-field correction on the order of  $\sim 1.5\%$ , might produce an artificial secondary signal with a period close to 24/4 hr. Then, the apparent secondary light-curve period of  $6.05 \pm 0.03$  hr might not be a detection of a real secondary rotation period (or its half) but rather an observational artifact repeating with the integer fraction of Earth’s rotation period for the observations taken from one station and during the same UT hour intervals on nearby nights. Though we do not have any direct evidence for or against the presence of this or other systematic errors in the GTC observations, we have to be cautious and require a confirmation of the suggested  $a_2/b_2$  estimates.

We conclude that the photometric observations obtained so far have not yet brought a trustworthy estimate for Dimorphos’s equatorial axis ratio. The signal from the secondary rotation is diluted in the light of the much larger primary, and its amplitude in the combined primary+secondary light curve is comparable to or lower than the photometric errors of the observations obtained during 2003–2021. To reveal Dimorphos’s rotational light curve and estimate its equatorial

<sup>35</sup> The large difference between the apparent secondary amplitudes seen on 2019 March 9–11 and 2021 January 14 could not be caused by a difference in viewing geometry, as the secondary was seen, assuming its spin pole is the same as the mutual orbit pole, at nearly the same aspect on both epochs. For the mutual orbit pole solution by Scheirich & Pravec (2022), the angle between the Earth–asteroid line and the Dimorphos equatorial plane was  $16^\circ 4'$  and  $16^\circ 8'$ , respectively, on the two epochs.

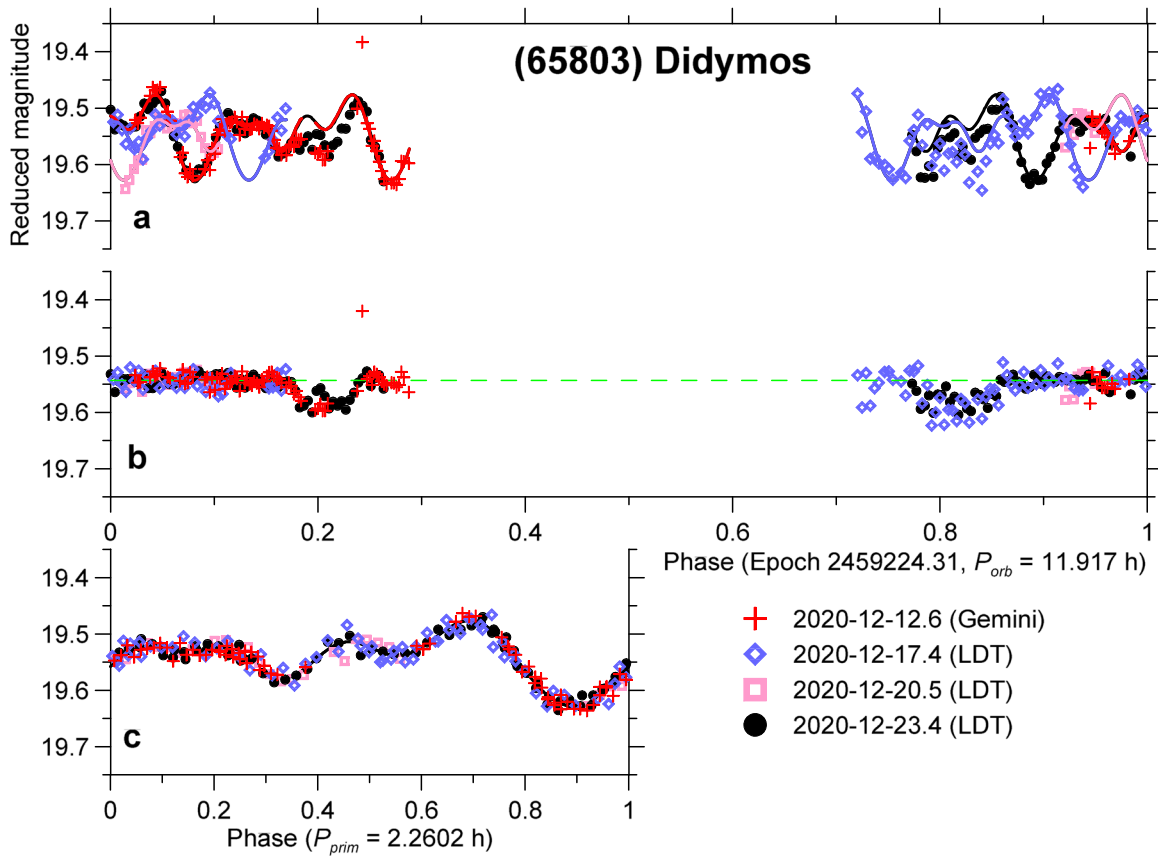


Figure 7. Didymos light curve from 2020 December 12 to 2020 December 23. See the caption of Figure 1 for a description of the content of the panels.

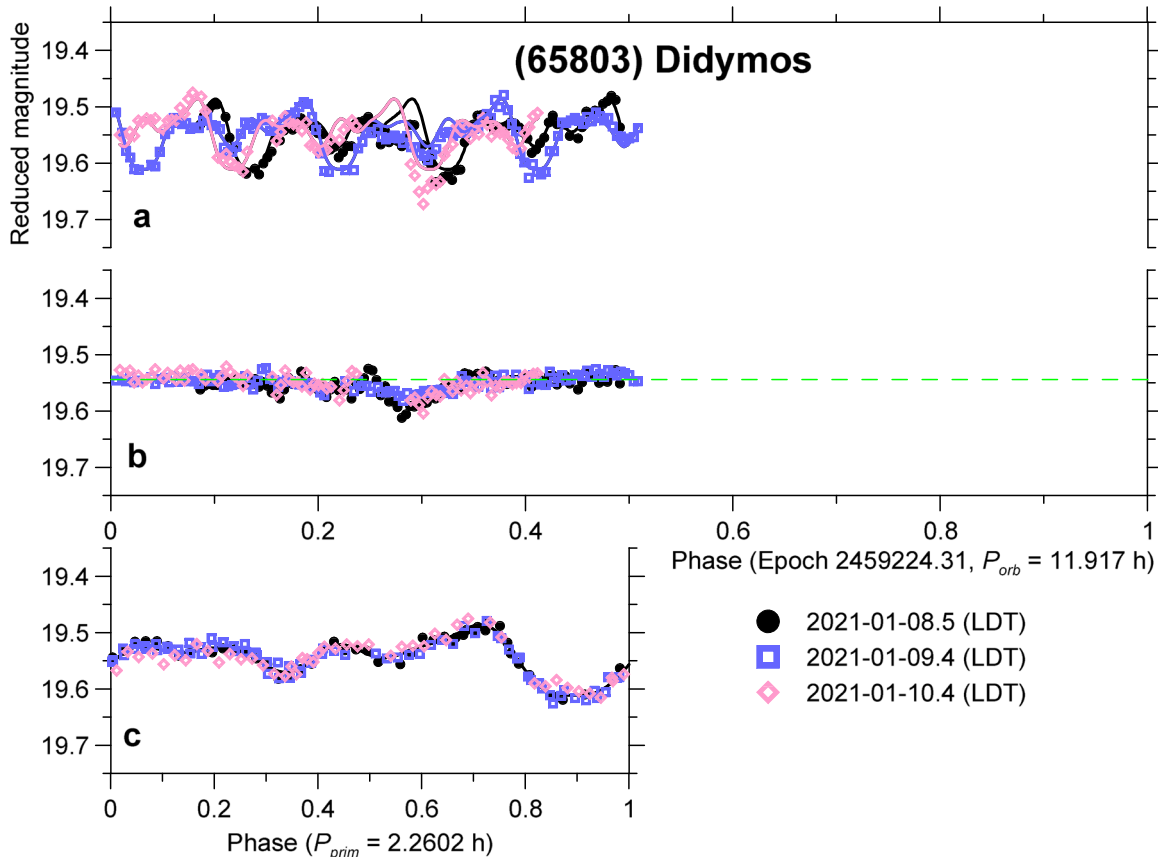
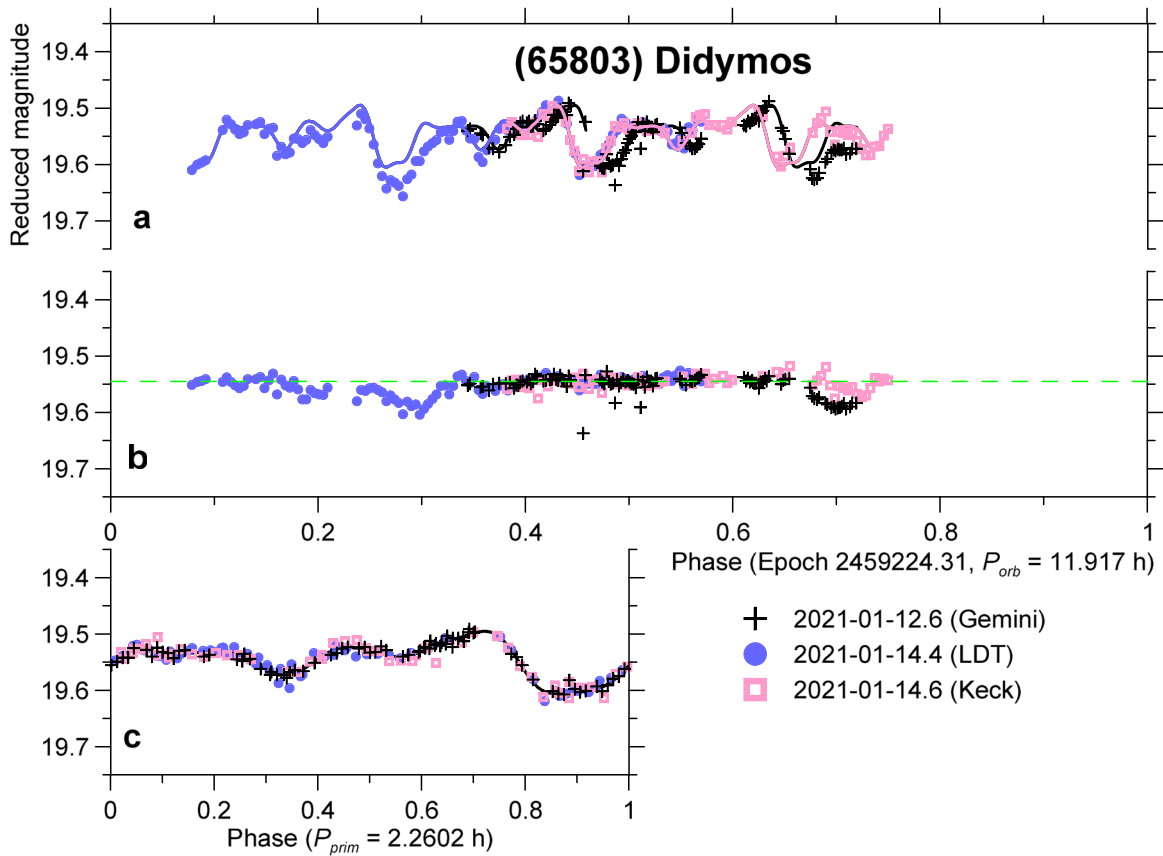
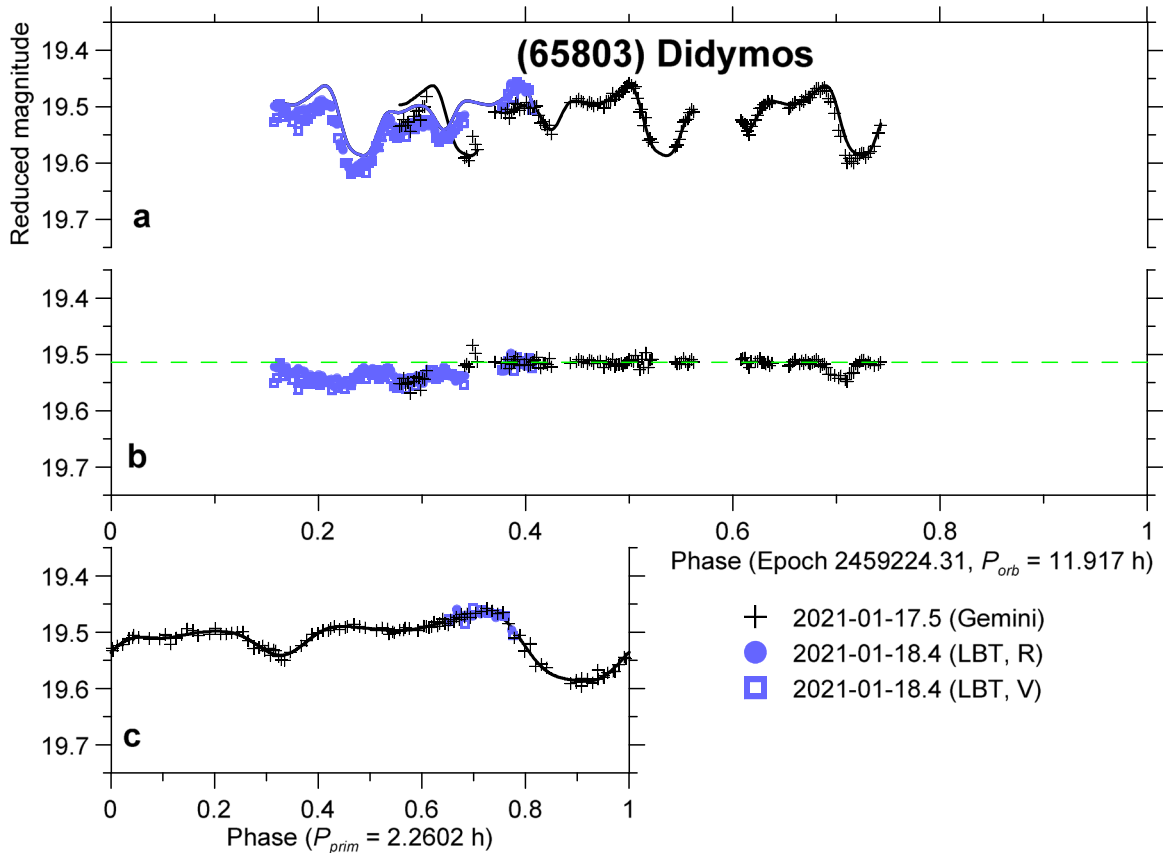


Figure 8. Didymos light curve from 2021 January 8 to 2021 January 10. See the caption of Figure 1 for a description of the content of the panels.

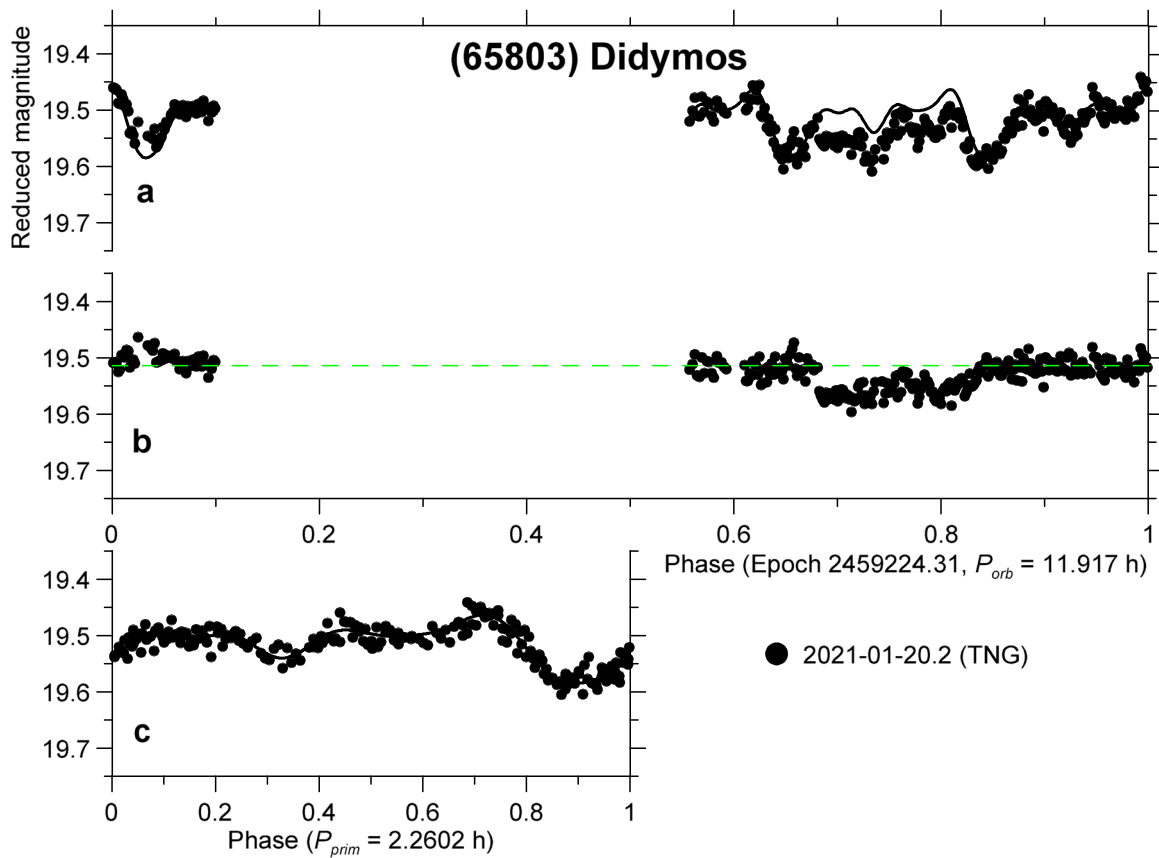




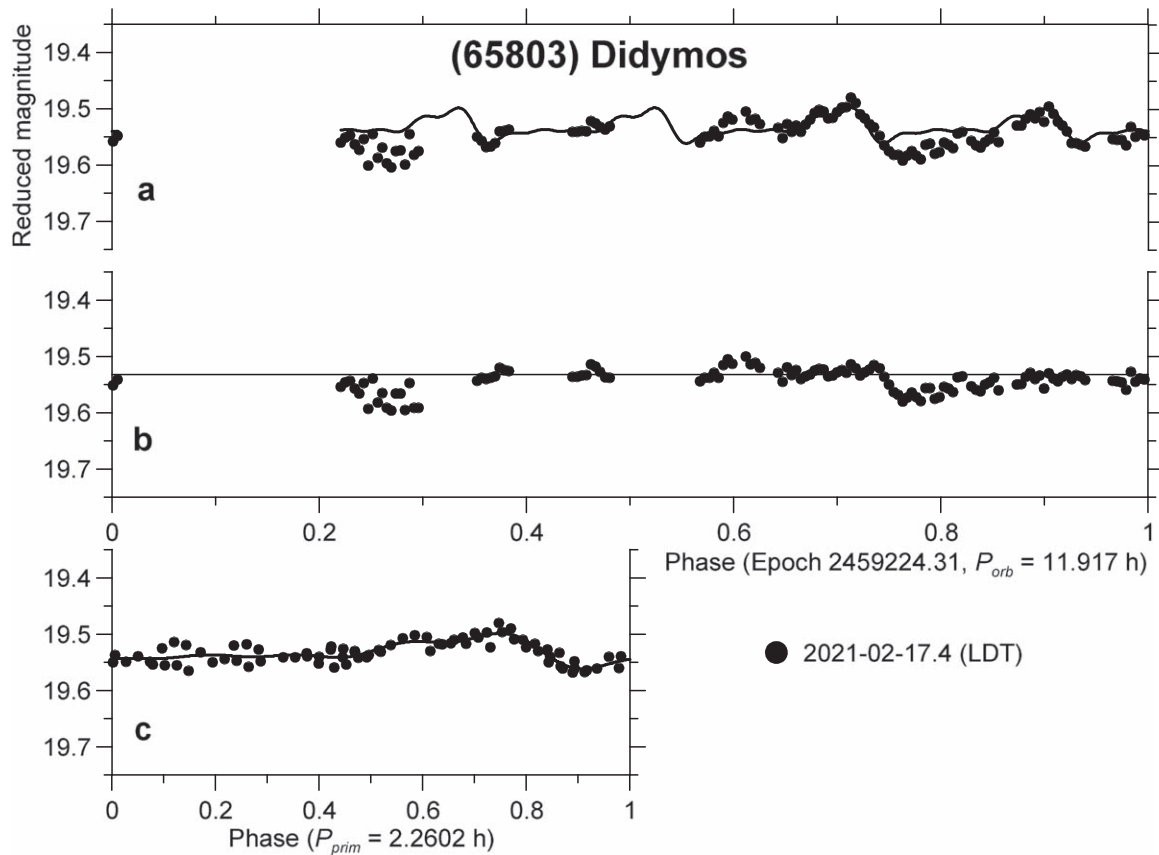
**Figure 9.** Didymos light curve from 2021 January 12 to 2021 January 14. See the caption of Figure 1 for a description of the content of the panels.



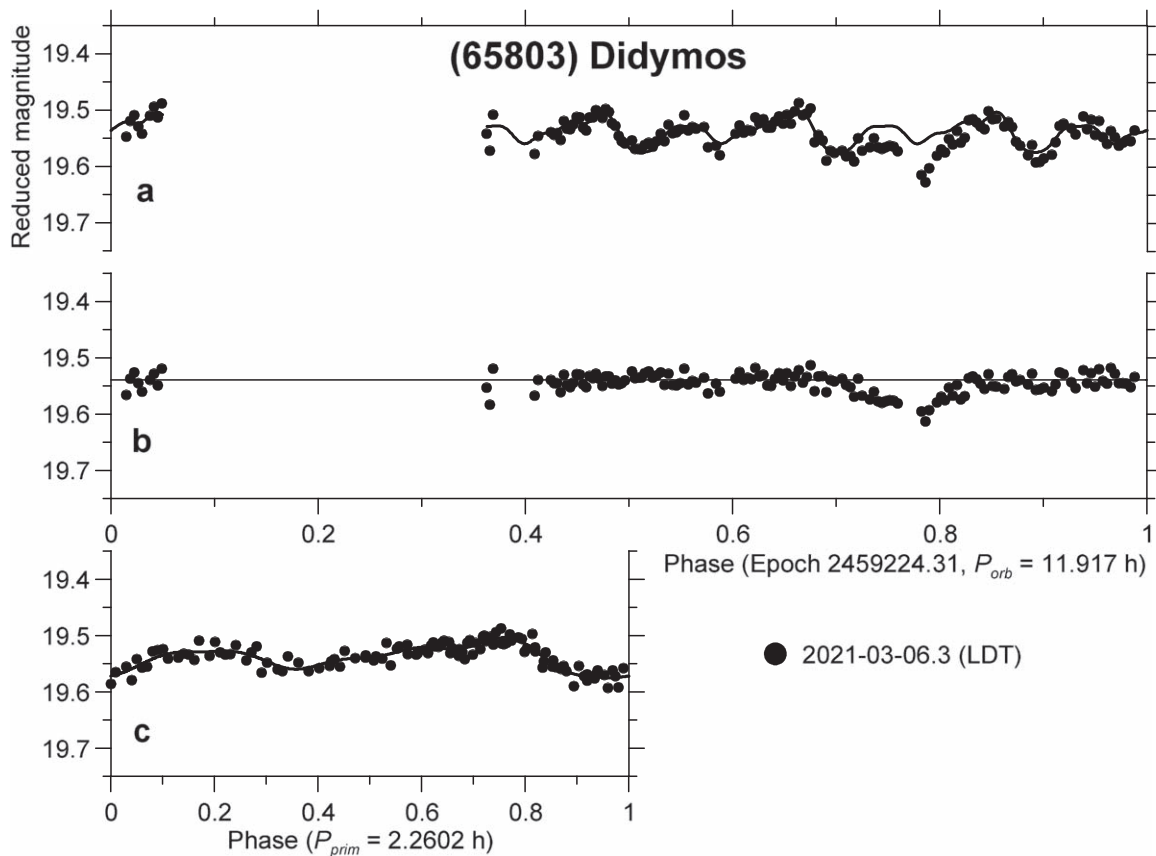
**Figure 10.** Didymos light curve from 2021 January 17 to 2021 January 18. See the caption of Figure 1 for a description of the content of the panels.



**Figure 11.** Didymos light curve from 2021 January 20. See the caption of Figure 1 for a description of the content of the panels.



**Figure 12.** Didymos light curve from 2021 February 17. See the caption of Figure 1 for a description of the content of the panels.



**Figure 13.** Didymos light curve from 2021 March 6. See the caption of Figure 1 for a description of the content of the panels.

elongation with a good degree of confidence, we will need to take very high quality observations with photometric errors, both random and systematic, of 0.005 mag or less. Taking such observations over at least half of Dimorphos's orbital period on at least 2 nights and with at least two different telescopes will probably be necessary to obtain confidence in the results for the secondary light curve by seeing a mutual consistency between the obtained data. While getting data with statistical errors of 0.005 mag will not be a problem with good telescopes when Didymos is bright ( $V = 14.5\text{--}18$ ) in 2022 July–September, it may be particularly demanding to control all potential systematic error sources to within 0.005 mag for the (relatively) fast-moving target over a 6 hr long nightly observing run.

## 5. Conclusions

The photometric observations performed for the Didymos binary asteroid system with 11 telescopes with diameters from 3.5 to 10.4 m in 2015–2021 provided detections of as many as 37 mutual occultation/eclipse events between the binary system components. The full photometric data set containing 55 mutual events, including the 18 detected in 2003 (Pravec et al. 2006), provides a great basis for modeling Dimorphos's orbit around the primary (Naidu et al. 2022; Scheirich & Pravec 2022). The decomposed primary light-curve data, which reveal a complex primary light-curve shape on some epochs, may be useful for refined primary shape modeling when combined with the 2003 radar and light-curve observations in the future. Detection of the secondary rotational light curve turned out to be challenging due to the relatively small size of Dimorphos, with the first estimates on the Dimorphos

equatorial axis ratio being mutually inconsistent. The observational requirements for obtaining a successful detection of the Dimorphos rotational light curve are given. These observations will be challenging but potentially doable when Didymos is bright in 2022 July–September.

The work by P.P. and P.S. was supported by the Grant Agency of the Czech Republic, grant 20-04431S. N.M. and A.T. acknowledge support from NASA NEOO grants NNX14AN82G and NNX17AH06G, awarded to the Mission Accessible Near-Earth Object Survey (MANOS). J.d.L. and J.L. acknowledge financial support from the NEO-MAPP project under grant agreement No. 870377. These results made use of the Lowell Discovery Telescope (LDT) at Lowell Observatory. Lowell is a private, nonprofit institution dedicated to astrophysical research and public appreciation of astronomy and operates the LDT in partnership with Boston University, the University of Maryland, the University of Toledo, Northern Arizona University, and Yale University. The Large Monolithic Imager was built by Lowell Observatory using funds provided by the National Science Foundation (AST-1005313). Based in part on observations collected at the European Southern Observatory under ESO programs 098.C-0793, 099.C-0075, and 0103.C-0282. Based in part on observations made with the Gran Telescopio Canarias, installed in the Spanish Observatorio del Roque de los Muchachos of the Instituto de Astrofísica de Canarias, on the island of La Palma, under programs GTC39/16B and GTC25/19A. The William Herschel Telescope is operated on the island of La Palma by the Isaac Newton Group of Telescopes in the Spanish Observatorio del Roque de los Muchachos of the Instituto de Astrofísica de Canarias. The WHT photometry was

made through program W/2017A/02. Based in part on observations obtained at the international Gemini Observatory (program IDs GN-2017A-FT-16, GN-2019A-FT-105, and GN-2020B-Q-209), a program of NSF’s NOIRLab, which is managed by the Association of Universities for Research in Astronomy (AURA) under a cooperative agreement with the National Science Foundation, on behalf of the Gemini Observatory partnership: the National Science Foundation (United States), National Research Council (Canada), Agencia Nacional de Investigación y Desarrollo (Chile), Ministerio de Ciencia, Tecnología e Innovación (Argentina), Ministério da Ciência, Tecnologia, Inovações e Comunicações (Brazil), and Korea Astronomy and Space Science Institute (Republic of Korea) and processed using the Gemini IRAF package. This work was enabled by observations made from the Gemini North telescope, located within the Maunakea Science Reserve and adjacent to the summit of Maunakea. We are grateful for the privilege of observing the universe from a place that is unique in both its astronomical quality and its cultural significance. We thank Dr. Mark Jesus Mendoza Magbanua (University of California San Francisco), Jay Kueny (Steward Observatory, Lowell Observatory), and Prof. David Trilling (NAU) for their encouragement and support during the data reduction phase of this work. We thank Prof. Mike Gowanlock (NAU) for his insights into parallel computing and Monsoon cluster administrator Christopher Coffey (NAU) and the High Performance Computing Support team for facilitating the computational needs during the photometry phase of this work. This material is based upon work supported by the National Science Foundation Graduate Research Fellowship Program under grant No. 2018258765. C.O.C. and C.A.T. also acknowledge support from the NASA Solar System Observations program (grant 80NSSC19K0869). Computational analyses were run on Northern Arizona University’s Monsoon computing cluster, funded by Arizona’s Technology and Research Initiative Fund. This work was made possible in part through the State of Arizona Technology and Research Initiative Program. World Coordinate System (WCS) corrections were facilitated by the *Astrometry.net* software suite. We thank R. Vervack for helping to prepare for and participating in the Keck observations. The Telescopio Nazionale Galileo is operated on the island of La Palma by the Centro Galileo Galilei of the Istituto Nazionale di Astrofisica (INAF) at the Spanish Observatorio del Roque de los Muchachos of the Instituto de Astrofísica de Canarias. The observations of Didymos were obtained within the program TNG AOT42\_8. E. M.E., E.D., S.I., and M.D. acknowledge funding by the Agenzia Spaziale Italiana (ASI) under A.A. No. 2019-31-HH.0. D.S. thanks the Action Fédératrice “ESTERS—Environnement Spatial de la Terre: Recherche & Surveillance” of the Paris Observatory for financial support. Funding for SDSS-III has been provided by the Alfred P. Sloan Foundation, the Participating Institutions, the National Science Foundation, and the U.S. Department of Energy Office of Science. The SDSS-III website is <http://www.sdss3.org/>. The SDSS-III is managed by the Astrophysical Research Consortium for the Participating Institutions of the SDSS-III Collaboration, including the University of Arizona, the Brazilian Participation Group, Brookhaven National Laboratory, Carnegie Mellon University, the University of Florida, the French Participation Group, the German Participation Group, Harvard University, the Instituto de Astrofísica de Canarias, the Michigan State/Notre Dame/JINA Participation Group, Johns Hopkins University, Lawrence

Berkeley National Laboratory, the Max Planck Institute for Astrophysics, the Max Planck Institute for Extraterrestrial Physics, New Mexico State University, New York University, Ohio State University, Pennsylvania State University, the University of Portsmouth, Princeton University, the Spanish Participation Group, the University of Tokyo, the University of Utah, Vanderbilt University, the University of Virginia, the University of Washington, and Yale University.

## Appendix A Fourier Series Coefficients of Didymos Light-curve Decompositions

In Table A1, we present the coefficients of the best-fit Fourier series (Equation (1)) of the 13 light-curve decompositions presented in Section 3. For each data set, the table gives the periods, the epoch (the zero-point time in the astero-centric frame, i.e., with the times corrected for light-travel time, Julian Date;  $t_0$ ), the mean light level (corresponding to  $C_0$ ) on the relative magnitude scale for each individual data set, and the normalized Fourier coefficients for the individual orders (up to the maximum significant order; see Section 3). In two cases—the data sets of 2019 March 9–11 and 2021 January 12 to 2021 January 14—we present the fits done with setting  $P_2 = 5.9585$  hr, i.e., at half of the assumed synchronous synodic secondary rotation period, as there was apparently a (marginally) significant secondary rotational light-curve signal (see the analysis in Section 4).

**Table A1**  
Fourier Series Coefficients of Didymos Light-curve Decompositions

	$j$	$k$	$C_{jk}/C_0$	$S_{jk}/C_0$
Data 2015-4-13 to 2015-4-14 (Figure 1)				
$P_1 = 2.2593$ hr				
$P_2 = 11.91$ hr				
Epoch = 2,457,126.05				
Mean level (mag) = $-2.2440$				
	1	1	0.0130	$-0.0056$
	1	2	0.0103	0.0078
	1	3	$-0.0056$	$-0.0086$
	1	4	0.0005	$-0.0029$
	1	5	0.0077	$-0.0046$
	1	6	0.0019	$-0.0017$
	1	7	$-0.0041$	0.0063
	1	8	$-0.0062$	0.0034
Data 2017-2-23 to 2017-3-1 (Figure 2)				
$P_1 = 2.2600$ hr				
$P_2 = 11.917$ hr				
Epoch = 2,457,809.58				
Mean level (mag) = 18.1804				
	1	1	$-0.0227$	$-0.0078$
	1	2	0.0012	0.0189
	1	3	$-0.0026$	0.0125
	1	4	0.0105	$-0.0016$
	1	5	$-0.0023$	0.0036
	1	6	0.0020	0.0014
	1	7	0.0043	0.0031
Data 2017-3-31 to 2017-4-2 (Figure 3)				
$P_1 = 2.2600$ hr				
$P_2 = 11.917$ hr				
Epoch = 2,457,809.58				
Mean level (mag) = 18.1941				
	1	1	$-0.0119$	$-0.0100$

**Table A1**  
(Continued)

	$j$	$k$	$C_{jk}/C_0$	$S_{jk}/C_0$
	1	2	-0.0139	0.0206
	1	3	-0.0038	-0.0002
	1	4	0.0018	-0.0026
	1	5	0.0077	-0.0015
	1	6	-0.0117	0.0055

Data 2017-4-18 to 2017-5-4 (Figure 4)

 $P_1 = 2.2600$  hr $P_2 = 11.917$  hr

Epoch = 2,457,809.58

Mean level (mag) = 18.1969

	1	1	-0.0061	-0.0226
	1	2	-0.0180	-0.0024
	1	3	-0.0118	-0.0074
	1	4	-0.0011	-0.0007
	1	5	0.0053	0.0019
	1	6	0.0032	0.0011
	1	7	0.0003	0.0076

Data 2019-1-31 to 2019-2-2 (Figure 5)

 $P_1 = 2.2600$  hr $P_2 = 11.917$  hr

Epoch = 2,458,514.96

Mean level (mag) = 19.0530

	1	1	0.0150	0.0113
	1	2	-0.0190	0.0169
	1	3	0.0093	-0.0066
	1	4	0.0050	0.0092
	1	5	0.0029	0.0010
	1	6	0.0017	-0.0027
	1	7	0.0026	0.0021

Data 2019-3-9 to 2019-3-11 (Figure 6)

 $P_1 = 2.2600$  hr $P_2 = 5.9585$  hr

Epoch = 2,458,552.82

Mean level (mag) = 19.0618

	1	1	0.0141	0.0136
	1	2	-0.0134	0.0082
	1	3	0.0066	0.0016
	1	4	0.0019	0.0024
	1	5	-0.0018	-0.0005
	1	6	0.0016	-0.0007
	1	7	-0.0010	0.0009
	1	8	0.0003	-0.0012
	1	9	-0.0004	0.0017
	2	1	-0.0069	0.0049

Data 2020-12-12 to 2020-12-23 (Figure 7)

 $P_1 = 2.2602$  hr $P_2 = 11.917$  hr

Epoch = 2,459,224.31

Mean level (mag) = 19.5426

	1	1	-0.0216	0.0000
	1	2	-0.0078	0.0348
	1	3	0.0058	0.0199
	1	4	0.0116	-0.0090
	1	5	-0.0002	0.0075
	1	6	-0.0020	0.0010

Data 2021-1-8 to 2021-1-10 (Figure 8)

 $P_1 = 2.2602$  hr $P_2 = 11.917$  hr

Epoch = 2,459,224.31

Mean level (mag) = 19.5439

**Table A1**  
(Continued)

	$j$	$k$	$C_{jk}/C_0$	$S_{jk}/C_0$
	1	1	-0.0173	0.0013
	1	2	-0.0089	0.0287
	1	3	0.0061	0.0171
	1	4	0.0101	-0.0069
	1	5	0.0009	0.0049
	1	6	-0.0053	0.0024
	1	7	0.0022	0.0030

Data 2021-1-12 to 2021-1-14 (Figure 9)

 $P_1 = 2.2602$  hr $P_2 = 5.9585$  hr

Epoch = 2,459,224.31

Mean level (mag) = 19.5450

	1	1	-0.0161	-0.0009
	1	2	-0.0055	0.0258
	1	3	0.0034	0.0150
	1	4	0.0110	-0.0068
	1	5	-0.0010	0.0034
	1	6	-0.0044	0.0017
	1	7	0.0003	0.0030
	1	8	0.0017	0.0019
	2	1	0.0004	0.0037

Data 2021-1-17 to 2021-1-18 (Figure 10)

 $P_1 = 2.2602$  hr $P_2 = 11.917$  hr

Epoch = 2,459,224.31

Mean level (mag) = 19.5138

	1	1	-0.0242	-0.0003
	1	2	-0.0087	0.0266
	1	3	0.0009	0.0171
	1	4	0.0101	-0.0053
	1	5	0.0030	0.0024
	1	6	-0.0036	0.0024
	1	7	0.0009	0.0016
	1	8	0.0015	0.0018

Data 2021-1-20 (Figure 11)

 $P_1 = 2.2602$  hr $P_2 = 11.917$  hr

Epoch = 2,459,224.31

Mean level (mag) = 19.5146

	1	1	-0.0187	0.0013
	1	2	-0.0088	0.0244
	1	3	-0.0006	0.0183
	1	4	0.0102	-0.0048
	1	5	-0.0002	0.0022
	1	6	-0.0048	0.0012

Data 2021-2-17 (Figure 12)

 $P_1 = 2.2602$  hr $P_2 = 11.917$  hr

Epoch = 2,459,224.31

Mean level (mag) = 19.5325

	1	1	-0.0104	-0.0111
	1	2	-0.0088	0.0086
	1	3	0.0009	0.0049
	1	4	0.0040	0.0034
	1	5	0.0032	-0.0033

Data 2021-3-6 (Figure 13)

 $P_1 = 2.2602$  hr $P_2 = 11.917$  hr

Epoch = 2,459,224.31

Mean level (mag) = 19.5393

**Table A1**  
(Continued)

	$j$	$k$	$C_{jk}/C_0$	$S_{jk}/C_0$
	1	1	-0.0093	-0.0070
	1	2	-0.0147	0.0130
	1	3	-0.0072	0.0050
	1	4	0.0031	0.0022
	1	5	0.0017	-0.0003
	1	6	-0.0030	-0.0026

**ORCID iDs**

P. Pravec [ID](https://orcid.org/0000-0001-8434-9776) <https://orcid.org/0000-0001-8434-9776>  
 C. A. Thomas [ID](https://orcid.org/0000-0003-3091-5757) <https://orcid.org/0000-0003-3091-5757>  
 A. S. Rivkin [ID](https://orcid.org/0000-0002-9939-9976) <https://orcid.org/0000-0002-9939-9976>  
 P. Scheirich [ID](https://orcid.org/0000-0001-8518-9532) <https://orcid.org/0000-0001-8518-9532>  
 N. Moskovitz [ID](https://orcid.org/0000-0001-6765-6336) <https://orcid.org/0000-0001-6765-6336>  
 M. M. Knight [ID](https://orcid.org/0000-0003-2781-6897) <https://orcid.org/0000-0003-2781-6897>  
 C. Snodgrass [ID](https://orcid.org/0000-0001-9328-2905) <https://orcid.org/0000-0001-9328-2905>  
 J. de León [ID](https://orcid.org/0000-0002-0696-0411) <https://orcid.org/0000-0002-0696-0411>  
 J. Licandro [ID](https://orcid.org/0000-0002-9214-337X) <https://orcid.org/0000-0002-9214-337X>  
 A. Thirouin [ID](https://orcid.org/0000-0002-1506-4248) <https://orcid.org/0000-0002-1506-4248>  
 C. O. Chandler [ID](https://orcid.org/0000-0001-7335-1715) <https://orcid.org/0000-0001-7335-1715>  
 W. J. Oldroyd [ID](https://orcid.org/0000-0001-5750-4953) <https://orcid.org/0000-0001-5750-4953>  
 C. A. Trujillo [ID](https://orcid.org/0000-0001-9859-0894) <https://orcid.org/0000-0001-9859-0894>  
 S. A. Sheppard [ID](https://orcid.org/0000-0003-3145-8682) <https://orcid.org/0000-0003-3145-8682>  
 T. L. Farnham [ID](https://orcid.org/0000-0002-4767-9861) <https://orcid.org/0000-0002-4767-9861>  
 S. Ieva [ID](https://orcid.org/0000-0001-8694-9038) <https://orcid.org/0000-0001-8694-9038>  
 M. Dall’Ora [ID](https://orcid.org/0000-0001-8209-0449) <https://orcid.org/0000-0001-8209-0449>  
 R. Kokotanekova [ID](https://orcid.org/0000-0003-4617-8878) <https://orcid.org/0000-0003-4617-8878>  
 B. Carry [ID](https://orcid.org/0000-0001-5242-3089) <https://orcid.org/0000-0001-5242-3089>

**References**

- Ahn, C. P., Alexandroff, R., Allende Prieto, C., et al. 2012, *ApJS*, **203**, 21  
 Ahumada, R., Prieto, C. A., Almeida, A., et al. 2020, *ApJS*, **249**, 3  
 Appenzeller, I., Fricke, K., Fürtig, W., et al. 1998, *Msngr*, **94**, 1  
 Astropy Collaboration, Price-Whelan, A. M., Sipőcz, B. M., et al. 2018, *AJ*, **156**, 123  
 Bertin, E. 2006, in ASP Conf. Ser. 351, *Astronomical Data Analysis Software and Systems XV*, ed. C. Gabriel et al. (San Francisco, CA: ASP), 112  
 Bertin, E., & Armouts, S. 1996, *A&AS*, **117**, 393  
 Binzel, R. P., Rivkin, A. S., Stuart, J. S., et al. 2004, *Icar*, **170**, 259  
 Blanton, M. R., Bershady, M. A., Abolfathi, B., et al. 2017, *AJ*, **154**, 28  
 Bradley, L., Sipőcz, B., Robitaille, T., et al. 2017, *Astropy/Photutils: V0.4*, Zenodo. DOI:10.5281/zenodo.1039309  
 Buzzoni, B., Delabre, B., Dekker, H., et al. 1984, *Msngr*, **38**, 9  
 Cepa, J. 2010, in *Highlights of Spanish Astrophysics V*, *Astrophysics and Space Science Proc.*, ed. J. M. Diego & L. J. Goicoechea (Berlin: Springer-Verlag), 15  
 Cepa, J., Aguiar, M., Escalera, V. G., et al. 2000, *SPIE*, **4008**, 623  
 Chambers, K. C., Magnier, E. A., Metcalfe, N., et al. 2016, arXiv:1612.05560  
 Chandler, C. O., Curtis, A. M., Mommert, M., Sheppard, S. S., & Trujillo, A. A. 2018, *PASP*, **130**, 114502  
 Collins, K. A., Kielkopf, J. F., Stassun, K. G., & Hessman, F. V. 2017, *AJ*, **153**, 77  
 de León, J., Licandro, J., Duffard, R., & Serra-Ricart, M. 2006, *AdSpR*, **37**, 178  
 de León, J., Licandro, J., Serra-Ricart, M., Pinlla-Alonso, N., & Campins, H. 2010, *A&A*, **517**, A23  
 Dotto, E., Delal Corte, V., Amoroso, M., et al. 2021, *P&SS*, **199**, 105185  
 Dunn, T. L., Burbine, T. H., Bottke, W. F., Jr, & Clark, J. P. 2013, *Icar*, **222**, 273  
 Flewelling, H. A., Magnier, E. A., Chambers, K. C., et al. 2020, *ApJS*, **251**, 7  
 Gaia Collaboration, Brown, A. G. A., & Vallenari, A. 2018, *A&A*, **616**, A1  
 Gaia Collaboration, Brown, A. G. A., & Vallenari, A. 2021, *A&A*, **649**, A1  
 Hook, I. M., Jørgensen, I., Allington-Smith, J. R., et al. 2004, *PASP*, **116**, 425  
 Ieva, S., Mazzotta, E., Perna, D., et al. 2022, *PSJ*, in press  
 Kitazato, K., Abe, M., Mito, H., et al. 2004, *LPSC*, **35**, 1623  
 Kokotanekova, R., Snodgrass, C., Lacerda, P., et al. 2017, *MNRAS*, **471**, 2974  
 Laher, R. R., Gorjian, V., Rebull, L. M., et al. 2012, *PASP*, **124**, 737  
 Lang, D., Hogg, D. W., Mierle, K., Blanton, M., & Roweis, S. 2010, *AJ*, **139**, 1782  
 Le Fèvre, O., Sisse, M., Mancini, D., et al. 2003, *SPIE*, **4841**, 1670  
 Lupton, R. H., Jurić, M., Ivezić, Z., et al. 2005, *BAAS*, **37**, 1384  
 Magnusson, P., Dahlgren, M., Barucci, M. A., et al. 1995, *Icar*, **123**, 227  
 Michel, P., Küppers, M., Campo Bagatin, A., et al. 2022, *PSJ*, **3**, 160  
 Mommert, M. 2017, *A&C*, **18**, 47  
 Naidu, S. P., Benner, L. A. M., Brozovic, M., et al. 2020, *Icar*, **348**, 113777  
 Naidu, S. P., Chesley, S. R., Farnocchia, D., et al. 2022, *PSJ*, submitted  
 Ochsenbein, F., Bauer, P., & Marcourt, J. 2000, *A&AS*, **143**, 23  
 Pravec, P., & Harris, A. W. 2007, *Icar*, **190**, 250  
 Pravec, P., Šarounová, L., & Wolf, M. 1996, *Icar*, **124**, 471  
 Pravec, P., Šarounová, L., Rabinowitz, D. L., et al. 2000, *Icar*, **146**, 190  
 Pravec, P., Benner, L. A. M., Nolan, M. C., et al. 2003, *IAUC*, **8244**, 2  
 Pravec, P., Harris, A. W., Scheirich, P., et al. 2006, *Icar*, **181**, 63  
 Pravec, P., Scheirich, P., Kušnirák, P., et al. 2016, *Icar*, **267**, 267  
 Rivkin, A. S., Chabot, N. L., Stickle, A. M., et al. 2021, *PSJ*, **2**, 173  
 Scheirich, P., & Pravec, P. 2009, *Icar*, **200**, 531  
 Scheirich, P., & Pravec, P. 2022, *PSJ*, **3**, 163  
 Schirmer, M. 2013, *ApJS*, **209**, 21  
 Snodgrass, C., Saviane, I., Monaco, L., & Sinclair, P. 2008, *Msngr*, **132**, 18  
 Stetson, P. B. 1987, *PASP*, **99**, 191  
 Stetson, P. B. 1990, *PASP*, **102**, 932  
 Stetson, P. B. 1993, in *IAU Coll. 136, Stellar Photometry—Current Techniques and Future Developments*, ed. C. J. Butler & I. Elliott (Cambridge: Cambridge Univ. Press), 291  
 Taylor, M. B. 2006, in ASP Conf. Ser. 351, *Astronomical Data Analysis Software and Systems XV*, ed. C. Gabriel et al. (San Francisco, CA: ASP), 666  
 Thirouin, A., & Sheppard, S. 2018, *AJ*, **155**, 248  
 Thirouin, A., Moskovitz, N. A., Binzel, R. P., et al. 2018, *ApJS*, **239**, 4  
 Tody, D. 1986, *SPIE*, **627**, 733  
 Tody, D. 1993, in ASP Conf. Proc. 52, *Astronomical Data Analysis Software and Systems II*, ed. R. J. Hanisch, R. J. V. Brissenden, & J. Barnes (San Francisco, CA: ASP), 173  
 Tonry, J. L., Stubbs, C. W., Lykke, K. R., et al. 2012, *ApJ*, **750**, 99  
 Zappalà, V., Cellino, A., Barucci, A. M., Fulchignoni, M., & Lupishko, D. F. 1990, *A&A*, **231**, 548